Published for SISSA by Springer

Received: June 3, 2024
Revised: July 25, 2024
Accepted: July 30, 2024
Published: August 29, 2024

Flavor dependence of unpolarized quark transverse momentum distributions from a global fit

The MAP collaboration[1]

Alessandro Bacchetta[a,b] **Valerio Bertone**[c] **Chiara Bissolotti**[d] **Giuseppe Bozzi**[e,f] **Matteo Cerutti**[g,h] **Filippo Delcarro**[a,b] **Marco Radici**[b] **Lorenzo Rossi**[a,b] **and Andrea Signori**[i,j]

[a] *Dipartimento di Fisica, Università di Pavia, via Bassi 6, Pavia I-27100, Italy*
[b] *INFN, Sezione di Pavia, via Bassi 6, Pavia I-27100, Italy*
[c] *IRFU, CEA, Université Paris-Saclay, Gif-sur-Yvette F-91191, France*
[d] *Argonne National Laboratory, Lemont, IL, U.S.A.*
[e] *Dipartimento di Fisica, Università di Cagliari, Cittadella Universitaria, Monserrato I-09042, CA, Italy*
[f] *INFN, Sezione di Cagliari, Cittadella Universitaria, Monserrato I-09042, CA, Italy*
[g] *Hampton University, Hampton, Virginia 23668, U.S.A.*
[h] *Jefferson Lab, Newport News, Virginia 23606, U.S.A.*
[i] *Dipartimento di Fisica, Università di Torino, via Pietro Giuria 1, Torino I-10125, Italy*
[j] *INFN, Sezione di Torino, via Pietro Giuria 1, Torino I-10125, Italy*

E-mail: alessandro.bacchetta@unipv.it, valerio.bertone@cea.fr, cbissolotti@anl.gov, giuseppe.bozzi@unica.it, mcerutti@jlab.org, filippo.delcarro@cern.ch, marco.radici@pv.infn.it, lorenzo.rossi@pv.infn.it, andrea.signori@unito.it

Abstract: We present an extraction of the unpolarized transverse-momentum-dependent parton distribution and fragmentation functions that takes into account possible differences between quark flavors and final-state hadrons. The extraction is based on experimental

[1] Multi-dimensional Analysis of Partonic distributions.

https://doi.org/10.1007/JHEP08(2024)232

JHEP08(2024)232

measurements from Drell-Yan processes and semi-inclusive deep-inelastic scattering, whose combination is essential to distinguish flavor differences. The analysis is carried out at N^3LL accuracy. The extracted flavor-dependent distributions give a very good description of the data ($\chi^2/N_{\rm dat} = 1.08$). The resulting error bands take fully into account also the uncertainties in the determination of the corresponding collinear distributions.

Keywords: Parton Distributions, Deep Inelastic Scattering or Small-x Physics, Specific QCD Phenomenology

ArXiv ePrint: 2405.13833

JHEP08(2024)232

Contents

1 Introduction

The transverse-momentum distributions (TMDs) provide insights into the three-dimensional structure of hadrons in momentum space, and are fundamental in understanding the world at the subatomic level. Thanks to the wealth of experimental measurements and the development of a robust theoretical framework, the study of TMDs has witnessed remarkable progress in recent years, and accurate phenomenological extractions for unpolarized quark TMDs in the proton are available [1–8]. TMDs were also studied in a different framework, the so called parton-branching approach [9–11]. The outcomes of these studies are partly available in the public `TMDlib` library [12, 13] (for a review, see also ref. [14]). Despite this advancement, there is still a lack of knowledge regarding the transverse momentum distribution of different quark flavors, and we are unable to clearly answer the question: do certain quark flavors carry more transverse momentum than others?

The question is legitimate because global extractions of collinear parton distribution functions (PDFs) clearly show that the distribution of longitudinal fractional momentum of partons strongly depends on their flavor (see ref. [15] for a recent review); similarly, for collinear fragmentation functions (FFs) [16, 17]. Moreover, there is no theoretical principle that prevents the transverse-momentum distribution of partons from having a similar behavior.

In this article, we aim to shed light on the variations in TMDs across different quark flavors. To achieve this goal, we compare theoretical predictions with experimental data from two

JHEP08(2024)232

distinct processes: Drell-Yan (DY) lepton-pair production and semi-inclusive deep-inelastic scattering (SIDIS). In relation to our goal, the two processes are highly complementary. On the one side, DY interactions do not involve hadrons in the final state and do not depend on TMD fragmentation functions (TMD FFs), but they offer valuable insight into TMD distribution functions (TMD PDFs) of quark-antiquark pairs. On the other side, SIDIS processes imply detecting final-state hadrons, and through TMD FFs they are particularly sensitive to flavor differences. The combination of these two processes is essential for our global analysis that incorporates for the first time all the necessary ingredients to reach a full N^{3}LL accuracy in the theoretical description of both DY and SIDIS processes. We remark also that TMDs depend on collinear PDFs and FFs: in this analysis, we take fully into account the uncertainties on these quantities by using all members of Monte Carlo PDF and FF sets. This procedure was already applied to DY in ref. [6] and is applied here for the first time to SIDIS. We obtain more realistic estimates of the uncertainties on the extracted TMDs.

In the literature, the problem of flavor-dependent TMDs has been addressed through models, lattice QCD calculations, and data-driven extractions. Some model calculations (see ref. [18] for a review) predict different TMDs for different quarks [19–25], although others do not [26–28]. The only pioneering work in lattice QCD on the subject indicates that down quarks carry higher transverse momentum than up quarks [29].

Earlier phenomenological extractions of flavor-dependent TMDs have been attempted in refs. [6, 8, 30]. Ref. [30] considered only a limited amount of data from SIDIS in a parton-model framework and concluded that there was room for a flavor dependence of TMDs, especially for the TMD FFs, but it was not possible to constrain it well, given the mentioned limitations. Refs. [6, 8] considered only data from DY, which has a reduced sensitivity to flavor differences.

By unraveling flavor-specific differences in transverse-momentum distributions, improving the theoretical accuracy of both DY and SIDIS cross sections to a full N^{3}LL level, and taking fully into account the uncertainties on collinear distributions, we take a significant step towards a more complete and precise understanding of the fundamental building blocks of matter. Our study not only contributes to the understanding of the internal structure of hadrons but also has broader implications for the interpretation of high-energy physics phenomena, such as the determination of the W mass in hadronic collisions [31–33]. It also paves the way for a deeper understanding of SIDIS experimental results at the future Electron-Ion Collider (EIC) [34–37].

2 Formalism

2.1 Drell-Yan

The inclusive Drell-Yan (DY) process

$$h_A(P_A) + h_B(P_B) \longrightarrow \gamma^*/Z(q) + X \longrightarrow \ell^+(l) + \ell^-(l') + X\,, \tag{2.1}$$

is the production of a lepton pair with four-momenta l, l' from the collision of two hadrons with four-momenta P_A, P_B via an intermediate neutral vector boson γ^*/Z with four-momentum q and large invariant mass $Q = \sqrt{q^2}$. The center-of-mass energy squared of the collision is $s = (P_A + P_B)^2$ and the conservation of momentum implies $q = l + l'$. The transverse

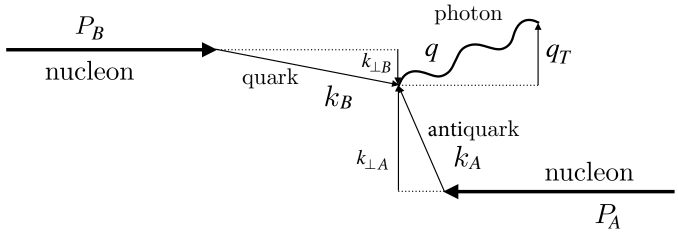

Figure 1. Diagram describing the relevant momenta involved in a DY event. In the collision of two nucleons with momenta P_A, P_B, a quark and an antiquark, with intrinsic (unmeasured) transverse momenta $\boldsymbol{k}_{\perp A}$ and $\boldsymbol{k}_{\perp B}$, annihilate and produce a virtual vector boson with (measured) transverse momentum $\boldsymbol{q}_T = \boldsymbol{k}_{\perp A} + \boldsymbol{k}_{\perp B}$ with respect to the collision axis.

momentum $|\boldsymbol{q}_T| = \sqrt{q_x^2 + q_y^2}$ of the intermediate boson with respect to the collision axis can be expressed in terms of the intrinsic transverse momenta of the incoming quarks $\boldsymbol{q}_T = \boldsymbol{k}_{\perp A} + \boldsymbol{k}_{\perp B}$, while its rapidity is given by $y = \ln \sqrt{\frac{q_0+q_z}{q_0-q_z}}$. The relevant kinematic quantities are schematically depicted in figure 1.

We are interested in the inclusive cross section differential with respect to the transverse momentum of the vector boson in the region of small $|\boldsymbol{q}_T|$ ($|\boldsymbol{q}_T| \ll Q$), which can be written as

$$\frac{d\sigma^{\mathrm{DY}}}{d|\boldsymbol{q}_T|\, dy\, dQ} = \frac{16\pi^2\alpha^2|\boldsymbol{q}_T|}{9Q^3}\, \mathcal{P}\, x_A\, x_B\, \mathcal{H}^{\mathrm{DY}}(Q,\mu) \sum_a c_a(Q^2) \times \int d^2\boldsymbol{k}_{\perp A}\, d^2\boldsymbol{k}_{\perp B}\, f_1^a(x_A, \boldsymbol{k}_{\perp A}^2; \mu, \zeta_A)\, f_1^{\bar{a}}(x_B, \boldsymbol{k}_{\perp B}^2; \mu, \zeta_B)\, \delta^{(2)}(\boldsymbol{k}_{\perp A} + \boldsymbol{k}_{\perp B} - \boldsymbol{q}_T)\,. \tag{2.2}$$

In the first line of eq. (2.2), α is the electromagnetic coupling, $\mathcal{P}$ is a phase-space-reduction factor accounting for possible lepton cuts,[1] $x_A = Qe^y/\sqrt{s}$ and $x_B = Qe^{-y}/\sqrt{s}$ are the longitudinal momentum fractions carried by the incoming partons, $\mathcal{H}^{\mathrm{DY}}$ is a perturbative hard factor encoding the virtual part of the scattering and depending on Q and on a renormalization scale μ. The sum runs over all active quark flavors and c_a are the electroweak charges given by

$$c_a(Q^2) = e_a^2 - 2e_a V_a V_\ell\, \chi_1(Q^2) + (V_\ell^2 + A_\ell^2)\,(V_a^2 + A_a^2)\, \chi_2(Q^2)\,, \tag{2.3}$$

with

$$\chi_1(Q^2) = \frac{1}{4\sin^2\theta_W \cos^2\theta_W} \frac{Q^2(Q^2 - M_Z^2)}{(Q^2 - M_Z^2)^2 + M_Z^2\Gamma_Z^2}\,, \tag{2.4}$$

$$\chi_2(Q^2) = \frac{1}{16\sin^4\theta_W \cos^4\theta_W} \frac{Q^4}{(Q^2 - M_Z^2)^2 + M_Z^2\Gamma_Z^2}\,, \tag{2.5}$$

where e_a, V_a, and A_a are the electric, vector, and axial charges of the flavor a, V_ℓ and A_ℓ are the vector and axial charges of the lepton ℓ, $\sin\theta_W$ is the weak mixing angle, M_Z and Γ_Z are mass and width of the Z boson. The second line of eq. (2.2) contains the convolution of the unpolarized TMDs f_1^a and $f_1^{\bar{a}}$, each one depending on the longitudinal and transverse

[1] See appendix C of ref. [5] for details.

momenta of the incoming quark/antiquark, and on the renormalization (μ) and rapidity (ζ) scales. The arbitrary choice made for the latter has to satisfy the kinematic constraint $\zeta_A\zeta_B = Q^4$: we will set $\mu^2 = \zeta_A = \zeta_B = Q^2$. Finally, the delta function in the second line of eq. (2.2) guarantees the conservation of transverse momentum.

The evolution of the TMD PDFs will be addressed in section 2.3. As usual, we work in the conjugate position space ($\boldsymbol{b}_T$ space) by defining the Fourier transform of the TMD PDFs:

$$\begin{aligned} \hat{f}_1^a(x, |\boldsymbol{b}_T|; \mu, \zeta) &= \int d^2\boldsymbol{k}_\perp \, e^{i\boldsymbol{b}_T\cdot\boldsymbol{k}_\perp} \, f_1^a(x, \boldsymbol{k}_\perp^2; \mu, \zeta) \\ &= 2\pi \int_0^\infty d|\boldsymbol{k}_\perp| \, |\boldsymbol{k}_\perp| J_0(|\boldsymbol{b}_T||\boldsymbol{k}_\perp|) \, f_1^a(x, \boldsymbol{k}_\perp^2; \mu, \zeta), \end{aligned} \tag{2.6}$$

where J_0 is the Bessel function of the first kind. This allows to rewrite the convolution in the second line of eq. (2.2) as

$$\frac{1}{2\pi} \int_0^{+\infty} d|\boldsymbol{b}_T||\boldsymbol{b}_T| J_0(|\boldsymbol{b}_T||\boldsymbol{q}_T|) \hat{f}_1^a(x_A, \boldsymbol{b}_T^2; \mu, \zeta_A) \, \hat{f}_1^{\bar{a}}(x_B, \boldsymbol{b}_T^2; \mu, \zeta_B). \tag{2.7}$$

2.2 Semi-inclusive deep-inelastic scattering

In the SIDIS process, a lepton with momentum l scatters off a hadron target N with mass M and four-momentum P, and the final state contains the scattered lepton with momentum l' and the hadron h with mass M_h and four-momentum P_h, i.e.,

$$\ell(l) + N(P) \to \ \ell(l') + h(P_h) + X \,. \tag{2.8}$$

The (space-like) four-momentum transfer $q = l - l'$, with $Q^2 \equiv -q^2 > 0$, is carried by a virtual photon and we consider the standard SIDIS kinematic invariants [38, 39]:

$$x = \frac{Q^2}{2\, P\cdot q}\,, \qquad y = \frac{P\cdot q}{P\cdot l}\,, \qquad z = \frac{P\cdot P_h}{P\cdot q}\,, \tag{2.9}$$

with $s = (P + l)^2$ the invariant mass squared of the process.

As for the transverse momenta, we consider the transverse component ($|\boldsymbol{P}_{hT}|$) of the final hadron momentum with respect to P and q or, equivalently, the transverse component ($|\boldsymbol{q}_T|$) of the virtual photon momentum with respect to P and P_h (see, for instance, refs. [40–42]). The two momenta are related by [43, 44]

$$q_T^\mu = -\frac{P_{hT}^\mu}{z} - 2x\frac{|\boldsymbol{q}_T|^2}{Q^2}P^\mu \approx -\frac{P_{hT}^\mu}{z}\,, \tag{2.10}$$

where the last approximation is valid assuming that the invariant mass of the photon is large compared to its transverse momentum ($|\boldsymbol{q}_T| \ll Q$) and the hadron masses involved in the process can be neglected. The relevant kinematic quantities are schematically depicted in figure 2.

We are interested in the hadron multiplicity, i.e., the differential number of hadrons of a given species h produced per corresponding inclusive DIS event:

$$M(x, z, |\boldsymbol{P}_{hT}| = z|\boldsymbol{q}_T|, Q) \ = \ \frac{1}{z}\frac{d\sigma^{\text{SIDIS}}}{dx\,dz\,d|\boldsymbol{q}_T|\,dQ}\Big/\frac{d\sigma^{\text{DIS}}}{dx\,dQ}\,. \tag{2.11}$$

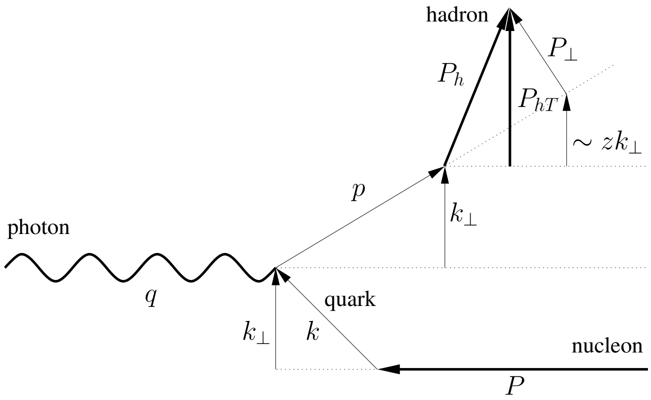

Figure 2. Diagram describing the relevant momenta involved in a SIDIS event in the Breit (nucleon-photon) frame. A virtual photon with momentum q (defining the reference axis) strikes a parton with momentum k and (unmeasured) transverse momentum $\boldsymbol{k}_\perp$ inside a nucleon with momentum P. The struck parton with momentum $p = k + q$ fragments into a hadron with momentum P_h, which acquires a further (unmeasured) transverse momentum $\boldsymbol{P}_\perp$ with respect to the fragmenting quark axis. The total (measured) transverse momentum of the final hadron is $\boldsymbol{P}_{hT}$. In the large Q^2 limit, $\boldsymbol{P}_{hT} \approx z\boldsymbol{k}_\perp + \boldsymbol{P}_\perp$.

The differential cross section at small transverse momenta, neglecting target mass corrections, reads [1, 38]

$$\begin{aligned}\frac{d\sigma^{\rm SIDIS}}{dx\,dz\,d|\boldsymbol{q}_T|\,dQ} &= \frac{8\pi^2\,\alpha^2\,z^2\,|\boldsymbol{q}_T|}{2\,x\,Q^3}\left[1+\left(1-\frac{Q^2}{xs}\right)^2\right] x\,\mathcal{H}^{\rm SIDIS}(Q,\mu)\sum_a e_a^2 \\ &\times \int d^2\boldsymbol{k}_\perp \int \frac{d^2\boldsymbol{P}_\perp}{z^2}\, f_1^a(x,\boldsymbol{k}_\perp^2;\mu,\zeta_A)\, D_1^{a\to h}(z,\boldsymbol{P}_\perp^2;\mu,\zeta_B)\,\delta^{(2)}(\boldsymbol{k}_\perp+\boldsymbol{P}_\perp/z+\boldsymbol{q}_T).\end{aligned} \tag{2.12}$$

In the first line of eq. (2.12), the sum runs over all active quark flavors. The hard factor $\mathcal{H}^{\rm SIDIS}$ is perturbatively computable and depends on Q and a renormalization scale μ. The second line contains the convolution of the unpolarized TMD PDF f_1^a as function of the rapidity scale ζ_A and of the transverse momentum $|\boldsymbol{k}_\perp|$ of the struck quark with respect to the nucleon axis, and the TMD FF $D_1^{a\to h}$ as function of the rapidity scale ζ_B and of the transverse momentum $|\boldsymbol{P}_\perp|$ of the produced hadron h with respect to the fragmenting quark axis.

Also in this case, it is convenient to work in the conjugate position ($\boldsymbol{b}_T$) space by defining the Fourier transform of the TMD FF:

$$\begin{aligned}\hat{D}_1^{a\to h}(z,\boldsymbol{b}_T^2;\mu,\zeta) &= \int \frac{d^2\boldsymbol{P}_\perp}{z^2}\, e^{-i\boldsymbol{b}_T\cdot\boldsymbol{P}_\perp/z}\, D_1^a(z,\boldsymbol{P}_\perp^2;\mu,\zeta) \\ &= 2\pi\int_0^\infty \frac{d|\boldsymbol{P}_\perp|}{z^2}\,|\boldsymbol{P}_\perp| J_0(|\boldsymbol{b}_T||\boldsymbol{P}_\perp|/z)\, D_1^a(z,\boldsymbol{P}_\perp^2;\mu,\zeta)\,.\end{aligned} \tag{2.13}$$

The convolution in the second line of eq. (2.12) can be rewritten as

$$\frac{1}{2\pi}\int_0^{+\infty} d|\boldsymbol{b}_T||\boldsymbol{b}_T| J_0(|\boldsymbol{b}_T||\boldsymbol{q}_T|)\,\hat{f}_1^a(x,\boldsymbol{b}_T^2;\mu,\zeta_A)\,\hat{D}_1^{a\to h}(z,\boldsymbol{b}_T^2;\mu,\zeta_B)\,. \tag{2.14}$$

In the TMD extraction of ref. [7], it was noted that a good description of low transverse-momentum SIDIS data can be achieved in a theoretical formalism where the TMD factorization formula contains the resummation of transverse-momentum logarithms up to the next-to-leading logarithmic (NLL) accuracy. However, it was also remarked that the quality of the description deteriorates when increasing the accuracy beyond NLL, because the predictions undershoot the data by approximately a q_T-independent factor.

In ref. [7], the problem was fixed by incorporating into the definition of the SIDIS multiplicity in eq. (2.11) the normalization factor

$$\omega(x,z,Q) = \frac{d\sigma^{\text{nomix}}}{dx\,dz\,dQ} \Bigg/ \int d^2\boldsymbol{q}_T\, W\,, \tag{2.15}$$

where the symbol W, commonly known as "W-term", denotes the differential cross section in eq. (2.12). In other words, the normalization factor ω is meant to compensate for all contributions in the collinear SIDIS cross section (numerator of eq. (2.15)) that are not included by simply integrating upon transverse momentum the corresponding differential SIDIS cross section (denominator of eq. (2.15)). The collinear SIDIS cross section includes only the terms that do not mix initial- and final-state contributions, hence the "nomix" label (see ref. [7] for a more complete explanation). Since in our theoretical framework we reach N^{3}LL accuracy (see section 2.3), we consistently include in the numerator terms up to second order in the strong coupling constant α_s, i.e. including $\mathcal{O}(\alpha_s^2)$ corrections as computed in ref. [45]. Alternative approaches to the normalization problem are available in the literature [46].

In conclusion, in our analysis we adopt the following expression for the fully differential SIDIS cross-section:

$$\frac{d\sigma_\omega^{\text{SIDIS}}}{dx\,dz\,d|\boldsymbol{q}_T|\,dQ} = \omega(x,z,Q)\,\frac{d\sigma^{\text{SIDIS}}}{dx\,dz\,d|\boldsymbol{q}_T|\,dQ}\,. \tag{2.16}$$

2.3 TMD evolution

The dependence of TMD PDFs and TMD FFs on the renormalization scale μ and the rapidity scale ζ arises from the removal of ultraviolet and rapidity divergences [47–49]. Each dependence is controlled by an evolution equation.[2] The complete set of equations (omitting the x and $\boldsymbol{b}_T$ dependencies for simplicity) is given by

$$\frac{\partial \hat{f}_1}{\partial \ln\mu} = \gamma(\mu,\zeta) \qquad \frac{\partial \hat{f}_1}{\partial \ln\sqrt{\zeta}} = K(\mu) \qquad \frac{\partial K}{\partial \ln\mu} = \frac{\partial\gamma}{\partial \ln\sqrt{\zeta}} = -\gamma_K(\alpha_s(\mu)) \tag{2.17}$$

where γ and K are the anomalous dimensions of the renormalisation-group and of the Collins-Soper evolution equations, respectively, and γ_K is the so-called cusp anomalous dimension.

Given a set of initial conditions at the scales $(\mu_i,\,\zeta_i)$, the solution to these differential equations allows us to determine the TMD at any final pair of scales $(\mu_f,\,\zeta_f)$. In addition, in the region of small $|\boldsymbol{b}_T|$ the TMD $\hat{f}_1$ can be matched onto its corresponding collinear PDF

[2] In this subsection, we briefly describe the evolution of TMD PDFs (an analogous description applies to TMD FFs): a more detailed treatment can be found in section 2 of ref. [5] (see also refs. [50, 51]).

JHEP08(2024)232

	$\mathcal{O}(\alpha_s^m)$ perturbative order				
Accuracy N^{n}LL	H and C	K and γ_F	γ_K	PDF and α_s evolution	FF evolution
NLL	0	1	2	LO	LO
N^{2}LL	1	2	3	NLO	NLO
N^{3}LL	2	3	4	NNLO	NNLO

Table 1. Logarithmic accuracies of the TMD evolution vs. $\mathcal{O}(\alpha_s^m)$ corrections in TMD ingredients.

f_1 through a convolution with suitable perturbative matching coefficients C. The resulting expression for the TMD PDF at the final scales $(\mu_f,\ \zeta_f)$ is

$$\hat{f}_1(x,\, \boldsymbol{b}_T;\, \mu_f, \zeta_f) = [C \otimes f_1]\,(x,\, \boldsymbol{b}_T;\, \mu_i, \zeta_i)\, \exp\left\{ K(\mu_i) \ln \frac{\sqrt{\zeta_f}}{\sqrt{\zeta_i}} + \int_{\mu_i}^{\mu_f} \frac{d\mu}{\mu} \left[\gamma_F(\alpha_s(\mu)) - \gamma_K(\alpha_s(\mu)) \ln \frac{\sqrt{\zeta_f}}{\mu} \right] \right\}, \tag{2.18}$$

where $\gamma_F(\alpha_s(\mu)) = \gamma(\mu, \mu^2)$. A convenient choice for the scales μ_i and ζ_i is $\mu_i = \sqrt{\zeta_i} \equiv \mu_b = 2e^{-\gamma_E}/|\boldsymbol{b}_T|$, with γ_E the Euler constant, since it avoids the insurgence of large logarithms in the rapidity evolution kernel K and the matching coefficients C.

A given accuracy in the resummation of large logarithms of $|\boldsymbol{b}_T|$ implies that each ingredient in eq. (2.18) must be computed to the perturbative accuracies summarized in table 1. After a careful benchmark of the perturbative expressions in our code against other well-known codes [52, 53], we introduced some small modifications in some of the ingredients at the N^{3}LL level compared to what we used in the MAPTMD22 extraction [7]. We stress that the present extraction incorporates for the first time all the necessary ingredients in the TMD PDFs and TMD FFs to reach a full N^{3}LL accuracy.

The introduction of μ_b as the initial scale of the TMD evolution implies a prescription to avoid hitting the QCD Landau pole in the large-$|\boldsymbol{b}_T|$ region ($|\boldsymbol{b}_T| \gtrsim 1/\Lambda_{\text{QCD}}$) and to smoothly match the TMD formula onto the fixed-order calculation at large transverse momentum ($|\boldsymbol{q}_T| \sim Q$) [54–56] in the small-$|\boldsymbol{b}_T|$ region ($|\boldsymbol{b}_T| \to 0$). Here, we adopt the same choice of refs. [1, 7] and we replace μ_b with $\mu_{b_*} = 2e^{-\gamma_E}/b_*$, where

$$b_*(|\boldsymbol{b}_T|, b_{\min}, b_{\max}) = b_{\max} \left(\frac{1 - e^{-|\boldsymbol{b}_T|^4/b_{\max}^4}}{1 - e^{-|\boldsymbol{b}_T|^4/b_{\min}^4}} \right)^{1/4}, \tag{2.19}$$

with

$$b_{\max} = 2e^{-\gamma_E}\,\text{GeV}^{-1} \approx 1.123\,\text{GeV}^{-1}, \qquad b_{\min} = 2e^{-\gamma_E}/\mu_f\,. \tag{2.20}$$

This choice guarantees that the new variable b_* rapidly saturates to $b_{\max}$ ($b_{\min}$) at large (small) values of $|\boldsymbol{b}_T|$ (see refs. [1, 7] for more details). At the same time, the upper limit $b_{\max}$ introduces power corrections scaling like $\mathcal{O}((\Lambda_{\text{QCD}}/|\boldsymbol{q}_T|)^k)$ [57], with $k > 0$, that in the region $|\boldsymbol{q}_T| \simeq \Lambda_{\text{QCD}}$ need to be accounted for by introducing nonperturbative corrections to the Collins-Soper kernel K and to the TMD formula of eq. (2.18). Following refs. [1, 7], we split the Collins-Soper kernel K into a perturbative part $K(b_*, \mu_{b_*})$ and a nonperturbative part $g_K(|\boldsymbol{b}_T|)$ that must vanish in the limit $|\boldsymbol{b}_T| \to 0$. The final expression for the evolved

TMD PDF is

$$\hat{f}_1(x, \boldsymbol{b}_T; \mu_f, \zeta_f) = [C \otimes f_1](x, \boldsymbol{b}_T; \mu_{b_*}, \mu_{b_*}^2)$$
$$\times \exp\left\{ K(b_*, \mu_{b_*}) \ln \frac{\sqrt{\zeta_f}}{\sqrt{\mu_{b_*}^2}} + \int_{\mu_{b_*}}^{\mu_f} \frac{d\mu}{\mu} \left[\gamma_F(\alpha_s(\mu)) - \gamma_K(\alpha_s(\mu)) \ln \frac{\sqrt{\zeta_f}}{\mu} \right] \right\} f_{1\,\mathrm{NP}}(x, \boldsymbol{b}_T; \zeta_f, Q_0)\,, \tag{2.21}$$

where $f_{1\,\mathrm{NP}}$ is a correction term that contains the nonperturbative part of the Collins-Soper kernel g_K, as well as other parameters (see section 4). The function $f_{1\,\mathrm{NP}}$ must satisfy the boundary condition $f_{1\,\mathrm{NP}} \to 1$ for $|\boldsymbol{b}_T| \to 0$, and it depends on an arbitrary scale Q_0 at which this correction is parametrized.

3 Analysis framework

3.1 Data

The set of experimental data used in the present analysis is identical to our previous MAPTMD22 global fit [7]. The total number of data points is 2031, of which 484 are from DY and 1547 from SIDIS measurements. In tables 2–3, we collect the relevant information on each data set. We emphasize that by combining data sets coming from a large number of different experimental collaborations, we are able to cover a wide range in the (x, Q^2) plane, as shown in figure 3.

In order to focus on the region of phase space relevant for the TMD formalism, it is necessary to impose appropriate kinematic cuts on the data set. For DY data, we consider vector-boson transverse momenta that satisfy $|\boldsymbol{q}_T| < 0.2\,Q$ to match the conditions for TMD factorization, and we further exclude the bins in Q that contain the Υ resonance. For SIDIS data, identifying the kinematic region where TMD factorization holds is more involved. First of all, we impose that $Q > 1.4\,\mathrm{GeV}$ in order to match the conditions for collinear QCD factorization. Moreover, we require that $0.2 < z < 0.7$ in order to include only data points in the SIDIS current fragmentation region and avoid contamination from exclusive processes. Finally, we adopt a kinematic cut in the detected hadron transverse momentum, $|\boldsymbol{P}_{hT}| < \min[\min[0.2Q, 0.5zQ] + 0.3\,\mathrm{GeV}, zQ]$. In this way, we can safely assume that $|\boldsymbol{q}_T| \ll Q$ without excluding too many bins, consistently with our previous study [7].

We refer to ref. [7] and references therein for more extensive details on the kinematic cuts and the treatment of systematic and statistical uncertainties.

3.2 Fit procedure

The agreement between our theoretical predictions and the experimental data is assessed by the usual χ^2 test,

$$\chi^2 = \sum_{i,j}^{N} (m_i - t_i) V_{ij}^{-1} (m_j - t_j)\,, \tag{3.1}$$

where m_i represents the experimental value for data point i, t_i denotes the corresponding theoretical prediction, and V_{ij} is the covariance matrix. When bin-by-bin correlated uncertainties

Experiment	N_{dat}	Observable	$\sqrt{s}$ [GeV]	Q [GeV]	y or x_F	Lepton cuts	Ref.
E605	50	$Ed^3\sigma/d^3\boldsymbol{q}$	38.8	7–18	$x_F = 0.1$	—	[58]
E772	53	$Ed^3\sigma/d^3\boldsymbol{q}$	38.8	5–15	$0.1 < x_F < 0.3$	—	[59]
E288 200 GeV	30	$Ed^3\sigma/d^3\boldsymbol{q}$	19.4	4–9	$y = 0.40$	—	[60]
E288 300 GeV	39	$Ed^3\sigma/d^3\boldsymbol{q}$	23.8	4–12	$y = 0.21$	—	[60]
E288 400 GeV	61	$Ed^3\sigma/d^3\boldsymbol{q}$	27.4	5–14	$y = 0.03$	—	[60]
STAR 510	7	$d\sigma/d\lvert\boldsymbol{q}_T\rvert$	510	73–114	$\lvert y\rvert < 1$	$p_{T\ell} > 25$ GeV $\lvert\eta_\ell\rvert < 1$	[61]
PHENIX200	2	$d\sigma/d\lvert\boldsymbol{q}_T\rvert$	200	4.8–8.2	$1.2 < y < 2.2$	—	[62]
CDF Run I	25	$d\sigma/d\lvert\boldsymbol{q}_T\rvert$	1800	66–116	Inclusive	—	[63]
CDF Run II	26	$d\sigma/d\lvert\boldsymbol{q}_T\rvert$	1960	66–116	Inclusive	—	[64]
D0 Run I	12	$d\sigma/d\lvert\boldsymbol{q}_T\rvert$	1800	75–105	Inclusive	—	[65]
D0 Run II	5	$(1/\sigma)d\sigma/d\lvert\boldsymbol{q}_T\rvert$	1960	70–110	Inclusive	—	[66]
D0 Run II (μ)	3	$(1/\sigma)d\sigma/d\lvert\boldsymbol{q}_T\rvert$	1960	65–115	$\lvert y\rvert < 1.7$	$p_{T\ell} > 15$ GeV $\lvert\eta_\ell\rvert < 1.7$	[67]
LHCb 7 TeV	7	$d\sigma/d\lvert\boldsymbol{q}_T\rvert$	7000	60–120	$2 < y < 4.5$	$p_{T\ell} > 20$ GeV $2 < \eta_\ell < 4.5$	[68]
LHCb 8 TeV	7	$d\sigma/d\lvert\boldsymbol{q}_T\rvert$	8000	60–120	$2 < y < 4.5$	$p_{T\ell} > 20$ GeV $2 < \eta_\ell < 4.5$	[69]
LHCb 13 TeV	7	$d\sigma/d\lvert\boldsymbol{q}_T\rvert$	13000	60–120	$2 < y < 4.5$	$p_{T\ell} > 20$ GeV $2 < \eta_\ell < 4.5$	[70]
CMS 7 TeV	4	$(1/\sigma)d\sigma/d\lvert\boldsymbol{q}_T\rvert$	7000	60–120	$\lvert y\rvert < 2.1$	$p_{T\ell} > 20$ GeV $\lvert\eta_\ell\rvert < 2.1$	[71]
CMS 8 TeV	4	$(1/\sigma)d\sigma/d\lvert\boldsymbol{q}_T\rvert$	8000	60–120	$\lvert y\rvert < 2.1$	$p_{T\ell} > 15$ GeV $\lvert\eta_\ell\rvert < 2.1$	[72]
CMS 13 TeV	70	$d\sigma/d\lvert\boldsymbol{q}_T\rvert$	13000	76–106	$\lvert y\rvert < 0.4$ $0.4 < \lvert y\rvert < 0.8$ $0.8 < \lvert y\rvert < 1.2$ $1.2 < \lvert y\rvert < 1.6$ $1.6 < \lvert y\rvert < 2.4$	$p_{T\ell} > 25$ GeV $\lvert\eta_\ell\rvert < 2.4$	[73]
ATLAS 7 TeV	6 6 6	$(1/\sigma)d\sigma/d\lvert\boldsymbol{q}_T\rvert$	7000	66–116	$\lvert y\rvert < 1$ $1 < \lvert y\rvert < 2$ $2 < \lvert y\rvert < 2.4$	$p_{T\ell} > 20$ GeV $\lvert\eta_\ell\rvert < 2.4$	[74]
ATLAS 8 TeV on-peak	6 6 6 6 6 6	$(1/\sigma)d\sigma/d\lvert\boldsymbol{q}_T\rvert$	8000	66–116	$\lvert y\rvert < 0.4$ $0.4 < \lvert y\rvert < 0.8$ $0.8 < \lvert y\rvert < 1.2$ $1.2 < \lvert y\rvert < 1.6$ $1.6 < \lvert y\rvert < 2$ $2 < \lvert y\rvert < 2.4$	$p_{T\ell} > 20$ GeV $\lvert\eta_\ell\rvert < 2.4$	[75]
ATLAS 8 TeV off-peak	4 8	$(1/\sigma)d\sigma/d\lvert\boldsymbol{q}_T\rvert$	8000	46–66 116–150	$\lvert y\rvert < 2.4$	$p_{T\ell} > 20$ GeV $\lvert\eta_\ell\rvert < 2.4$	[75]
ATLAS 13 TeV	6	$(1/\sigma)d\sigma/d\lvert\boldsymbol{q}_T\rvert$	13000	66–113	$\lvert y\rvert < 2.5$	$p_{T\ell} > 27$ GeV $\lvert\eta_\ell\rvert < 2.5$	[76]
Total	484						

Table 2. DY experimental data sets included in this global fit. Each row contains the number of data points (N_{dat}) after kinematic cuts, the measured observable, the center-of-mass energy $\sqrt{s}$, the invariant mass range, the angular variable (y or x_F), possible cuts on the final-state leptons, and the published reference.

JHEP08(2024)232

Experiment	N_{dat}	Observable	Channels	Q [GeV]	x	z	Phase space cuts	Ref.
HERMES	344	$M(x, z, \lvert \boldsymbol{P}_{hT} \rvert, Q)$	$p \to \pi^+$ $p \to \pi^-$ $p \to K^+$ $p \to K^-$ $d \to \pi^+$ $d \to \pi^-$ $d \to K^+$ $d \to K^-$	1–$\sqrt{15}$	$0.023 < x < 0.6$ (6 bins)	$0.1 < z < 1.1$ (8 bins)	$W^2 > 10\,\text{GeV}^2$ $0.1 < y < 0.85$	[77]
COMPASS	1203	$M(x, z, \boldsymbol{P}_{hT}^2, Q)$	$d \to h^+$ $d \to h^-$	1–9 (5 bins)	$0.003 < x < 0.4$ (8 bins)	$0.2 < z < 0.8$ (4 bins)	$W^2 > 25\,\text{GeV}^2$ $0.1 < y < 0.9$	[78]
Total	1547							

Table 3. SIDIS experimental data sets included in this global fit. Each row contains the number of data points (N_{dat}) after kinematic cuts, the measured observable, the SIDIS channel, the invariant mass range of the virtual photon, the covered ranges for the invariants x and z, possible cuts on the final-state lepton, and the published reference.

JHEP08(2024)232

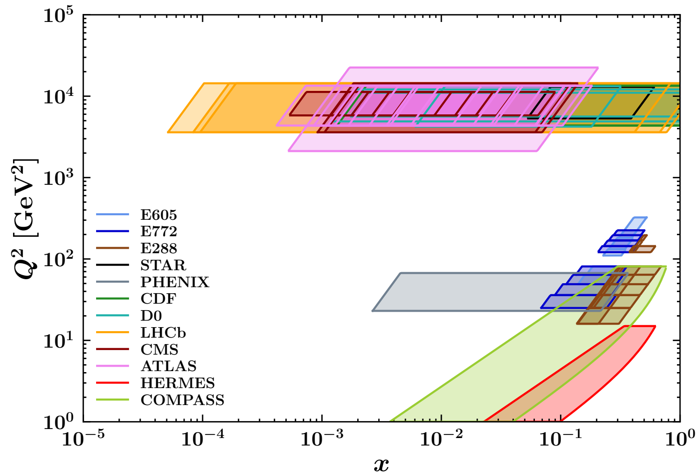

Figure 3. Coverage in the (x, Q^2) plane of the full experimental data set included in this global fit.

are present, the total χ^2 can be decomposed into two components [5, 7]:

$$\chi^2 = \sum_i^N \left(\frac{m_i - \bar{t}_i}{\sigma_i} \right)^2 + \chi_\lambda^2 = \chi_D^2 + \chi_\lambda^2 \,, \tag{3.2}$$

where χ_D^2 is given by the standard formula for N experimental data points with statistical and uncorrelated systematic uncertainties summed in quadrature, $\sigma_i^2 = \sigma_{i,\text{stat}}^2 + \sigma_{i,\text{uncor}}^2$, but involving theoretical predictions $\bar{t}_i$ for data point i shifted by the correlation uncertainties according to

$$\bar{t}_i = t_i + \sum_{\alpha=1}^{k} \lambda_\alpha \, \sigma_{i,\text{corr}}^{(\alpha)} \,, \tag{3.3}$$

where the sum runs upon the sources of correlated uncertainties, $\sigma^{(\alpha)}_{i,\mathrm{corr}}$ represents the α-th (fully) correlated uncertainty affecting the i-th experimental data point, and λ_α denotes the nuisance parameter. The term χ^2_λ in eq. (3.2) is a penalty contribution due to correlated uncertainties and it is entirely determined by the nuisance parameters:

$$\chi^2_\lambda = \sum_{\alpha=1}^{k} \lambda^2_\alpha \,. \tag{3.4}$$

The optimal values of the nuisance parameters are obtained by minimizing the total χ^2 in eq. (3.2) with respect to them. Since the shifted predictions in eq. (3.3) offer a better visual evaluation of the fit quality, we consistently present them for all observables employed in this global fit.

We performed the analysis by employing the so-called bootstrap method, which entails fitting a set of several Monte Carlo replicas of the data (100 in our case). Moreover, we use Monte Carlo sets for collinear PDFs and FFs and we change the member of the collinear sets for each replica. The most complete statistical information about the extracted TMDs is given by the full ensemble of replicas but, consistently with our previous work [7], we use as the most appropriate estimator of the fit quality the χ^2 value of the best fit for the *central* replica (χ^2_0), defined as the replica obtained by fitting experimental data without fluctuations.

4 Results

4.1 Flavor-independent nonperturbative parametrization

In this section, we describe our new simultaneous extraction of TMD PDFs and TMD FFs similar to the MAPTMD22 one [7], where the models for these two nonperturbative objects are considered the same for each quark flavor. This provides us with a reference to which the core results of this paper will be compared. The main innovation of this new extraction is the choice of the collinear PDF sets to build the TMDs: we use LHAPDF sets delivered as Monte Carlo ensembles [79]. This choice allows us to assign a specific member of the collinear sets to each TMD replica, which leads to a robust estimate of the uncertainty of the extracted TMD distributions, as already suggested in ref. [6]. We use the NNPDF3.1 set (NNPDF31_nnlo_pch_as_0118) [80] for PDFs, and a variation of the baseline MAPFF1.0 NNLO set [81] for FFs. The variation consists in the choice of the parametrization scale (1 GeV in our new set, 5 GeV in the baseline). In this way, we avoid complications related to backward evolution to the scale μ_b that appears in the expression of experimental observables in TMD factorization, because μ_b can be as low as 1 GeV.

Then, we repeat the analysis with the same settings but with a different approach for the model of TMD FFs. Specifically, we consider a more flexible model that separates the parametrization of the fragmentation of a quark into a pion from the one into a kaon. Such a separation was explored so far only in ref. [30]. In the following, we denote these two reference extractions as MAPTMD24 Flavor Independent (MAPTMD24 FI) and MAPTMD24 Hadron Dependent (MAPTMD24 HD).

JHEP08(2024)232

For both these analyses, the model of the nonperturbative part of the TMDs is the same as in the MAPTMD22 extraction [7]. Thus, the parametrization of TMD PDFs is

$$f_{1\,\mathrm{NP}}(x, \boldsymbol{b}_T^2; \zeta, Q_0) = \frac{g_1(x)\, e^{-g_1(x)\frac{\boldsymbol{b}_T^2}{4}} + \lambda^2\, g_2^2(x) \left[1 - g_2(x)\frac{\boldsymbol{b}_T^2}{4}\right] e^{-g_2(x)\frac{\boldsymbol{b}_T^2}{4}} + \lambda_2^2\, g_3(x)\, e^{-g_3(x)\frac{\boldsymbol{b}_T^2}{4}}}{g_1(x) + \lambda^2\, g_2^2(x) + \lambda_2^2\, g_3(x)} \left[\frac{\zeta}{Q_0^2}\right]^{g_K(\boldsymbol{b}_T^2)/2}, \tag{4.1}$$

corresponding to the Fourier transform of the sum of two Gaussians and a Gaussian weighted by $\boldsymbol{k}_\perp^2$.

The expression of the model for the TMD FFs is

$$D_{1\,\mathrm{NP}}(z, \boldsymbol{b}_T^2; \zeta, Q_0) = \frac{g_4(z)\, e^{-g_4(z)\frac{\boldsymbol{b}_T^2}{4z^2}} + \frac{\lambda_F}{z^2}\, g_5^2(z) \left[1 - g_5(z)\frac{\boldsymbol{b}_T^2}{4z^2}\right] e^{-g_5(z)\frac{\boldsymbol{b}_T^2}{4z^2}}}{g_4(z) + \frac{\lambda_F}{z^2}\, g_5^2(z)} \left[\frac{\zeta}{Q_0^2}\right]^{g_K(\boldsymbol{b}_T^2)/2}, \tag{4.2}$$

corresponding to the Fourier transform of the sum of a Gaussians and a Gaussian weighted by $\boldsymbol{P}_\perp^2$.

The g_i functions describe the widths of the distributions and include a dependence on x and z:

$$g_{\{1,2,3\}}(x) = N_{\{1,2,3\}} \frac{x^{\sigma_{\{1,2,3\}}} (1-x)^{\alpha^2_{\{1,2,3\}}}}{\hat{x}^{\sigma_{\{1,2,3\}}} (1-\hat{x})^{\alpha^2_{\{1,2,3\}}}}, \tag{4.3}$$

$$g_{\{4,5\}}(z) = N_{\{4,5\}} \frac{(z^{\beta_{\{1,2\}}} + \delta^2_{\{1,2\}})(1-z)^{\gamma^2_{\{1,2\}}}}{(\hat{z}^{\beta_{\{1,2\}}} + \delta^2_{\{1,2\}})(1-\hat{z})^{\gamma^2_{\{1,2\}}}}, \tag{4.4}$$

where $\hat{x} = 0.1$, $\hat{z} = 0.5$, and N_i ($i = 1-5$), σ_j, α_j ($j = 1$–3), β_i, δ_i, γ_i ($i = 1, 2$), are free parameters.

Finally, the nonperturbative part of the Collins-Soper kernel is parametrized as

$$g_K(\boldsymbol{b}_T^2) = -g_2^2\, \frac{\boldsymbol{b}_T^2}{2}. \tag{4.5}$$

This function governs the nonperturbative contribution $(\zeta_f/Q_0^2)^{g_K/2}$ to the TMD evolution, where Q_0 is the scale at which this contribution is parametrized; we set $Q_0 = 1\,\mathrm{GeV}$.

The functional forms in eqs. (4.1)–(4.4) are largely arbitrary. We choose to parametrize the nonperturbative parts of TMDs in terms of Gaussians and weighted Gaussians in transverse-momentum space because they are guaranteed to be positive at the initial scale $Q_0 = 1\,\mathrm{GeV}$. The widths of the Gaussians, expressed by eqs. (4.3)–(4.4), depend on x or z and vanish as x or z approach one. Our choice of the functional form is also inspired by model calculations of TMD PDFs (see, e.g., refs. [18, 19, 26, 28, 82–85]) and TMD FFs (see, e.g., refs. [24, 86]). Many of these models predict the existence of terms that behave similarly to Gaussians and weighted Gaussians. The details of their functional dependence are related to the correlation between the spin of the quarks and their transverse momentum. In the case of fragmentation functions, a different role can be played by different fragmentation channels. For example, a pion in the final state can be produced by the direct fragmentation of the active quark

	Data set $\chi_0^2/N_{\rm dat}$		
Collinear sets	DY total	SIDIS total	**Total**
MMHT + DSS (MAPTMD22)	1.66	0.87	**1.06**
NNPDF + DSS	1.62	0.90	**1.07**
MMHT + MAPFF	1.58	1.33	**1.39**
NNPDF + MAPFF (MAPTMD24 FI)	1.58	1.34	**1.40**
NNPDF + MAPFF (MAPTMD24 HD)	1.57	1.08	**1.19**

Table 4. Breakdown of the values of $\chi_0^2/N_{\rm dat}$ for different choices of collinear PDF and FF sets.

in the hard process, or by the decay of hadronic resonances, such as the ρ meson. The interplay of these two channels can generate different nontrivial features in the shape of the extracted TMD FFs.

After trying several parameter configurations, we noticed that it is possible to set $\sigma_2 = \sigma_3$ in eq. (4.3) without deteriorating the quality of the fit. With this last assumption, the fit involves 20 free parameters: 10 for the nonperturbative part of the TMD PDFs, 9 for the nonperturbative part of the TMD FFs, and 1 for the nonperturbative part of the Collis-Soper kernel.

We fitted 100 Monte Carlo replicas of the experimental data. We obtain for the central replica a χ^2 per data point $\chi_0^2/N_{\rm dat} = 1.40$. This result is not compatible with the one of the MAPTMD22 extraction ($\chi_0^2/N_{\rm dat} = 1.06$). In order to understand the origin of this deterioration, we investigated the impact of different combinations of collinear PDFs (MMHT2014 [87] and NNPDF3.1 [80]) and FFs (DSS14-17 [88, 89] and MAPFF1.0 [81]). In table 4, we report the values of $\chi_0^2/N_{\rm dat}$ for each scenario.

The results in table 4 clearly show that a change in the collinear PDF set from MMHT to NNPDF produces a negligible effect on the quality of the fit. This is reasonable because in the kinematic region covered by the global dataset included in this analysis the two considered PDF sets are well constrained and compatible with each other.[3]

In contrast, our results are significantly affected by the choice of collinear FFs. In fact, the $\chi_0^2/N_{\rm dat}$ becomes larger when moving from DSS to MAPFF. Unsurprisingly, this deterioration affects the description of SIDIS data, without significant impact on the description of Drell-Yan data. The increase of the $\chi_0^2/N_{\rm dat}$ value is mostly due to the MAPFF collinear set being affected by lower uncertainties as compared to the DSS one.

In figure 4, we show the unpolarized TMD PDFs of the up quark in a proton extracted in MAPTMD22 (orange) and MAPTMD24 FI (purple) as functions of the partonic transverse momentum $|\boldsymbol{k}_\perp|$ at $\mu = \sqrt{\zeta} = Q = 2\,\text{GeV}$ and $x = 0.1$ (left panel), and $\mu = \sqrt{\zeta} = Q = 100\,\text{GeV}$ and $x = 0.001$ (right panel). The plots evidently show that the TMD PDFs extracted with two different choices of collinear PDF sets are compatible with each other in the kinematic region covered by experimental data. We note that the MAPTMD24 uncertainty bands,

[3]We remark that in ref. [6], where also other sets of PDFs were taken into account, the authors concluded that the choice of collinear PDF sets led to a significant difference in the description of experimental data and required a change in the functional form of the nonperturbative components.

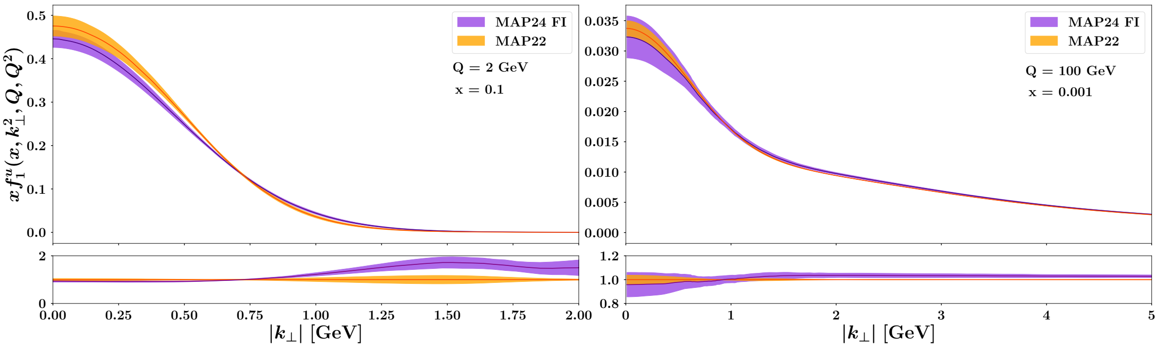

Figure 4. Comparison between the unpolarized TMD PDFs of the up quark in a proton extracted in the MAPTMD22 fit (orange) and the MAPTMD24 Flavor Independent fit (purple), as functions of the partonic transverse momentum $|\boldsymbol{k}_\perp|$ at $\mu = \sqrt{\zeta} = Q = 2\,\text{GeV}$, $x = 0.1$ (left panel) and $\mu = \sqrt{\zeta} = Q = 100\,\text{GeV}$, $x = 0.001$ (right panel). Lower panels show the ratio of MAPTMD24 Flavor Independent to MAPTMD22. The uncertainty bands represent the 68% C.L.

corresponding to the 68% confidence level (C.L.), are equal to or larger than the MAPTMD22 ones, as a consequence of the fact that each replica of the MAPTMD24 fit is associated to a different member of the collinear PDF set, while in the MAPTMD22 fit all TMD replicas were associated to the same member.

In figure 5, we display the unpolarized TMD FFs for an up quark fragmenting into a π^+ extracted in the MAPTMD22 (brown) and MAPTMD24 FI (light blue) fits, as functions of the pion transverse momentum $|\boldsymbol{P}_\perp|$ at $\mu = \sqrt{\zeta} = Q = 2\,\text{GeV}$ and $z = 0.4$ (left panel), and $z = 0.6$ (right panel). We note significant differences both in shape and normalization, which can be traced back to the different choice of the collinear FF set (see table 4). However, there was no need to change the functional form of the nonperturbative parametrization, since it turned out to be sufficiently flexible to accommodate the differences caused by changing the collinear FF set. The MAPTMD24 FI fragmentation function has a second smaller peak at intermediate $|\boldsymbol{P}_\perp|$, especially in the low-z region. This feature is present also in the MAPTMD22 fit, but the size of the peak is smaller and its position shifted to higher $|\boldsymbol{P}_\perp|$ values. As anticipated in model descriptions of fragmentation functions, this behavior could be induced by the interference of different channels in the fragmentation process where the detected hadron could be produced directly or through the decay of heavier resonances. The TMD FFs could be better constrained by data from double-inclusive hadron production in electron-positron annihilation [90]. Important constraints could be obtained also from different processes, such as single-inclusive hadron production in electron-positron annihilation with the reconstruction of the thrust or jet axis [91–94].

Since the flavor-independent ansatz for the nonperturbative part of TMDs does not provide a sufficiently good description of the data, as an intermediate step toward a flavor-dependent extraction we consider a flavor-independent but hadron-dependent ansatz. Namely, we allow the non-perturbative parts of the TMD FF for pions to differ from those for kaons. We employ the same functional form of eq. (4.2) but with different parameters for pions and kaons. In this version of the extraction, denoted as MAPTMD24 HD, we have a total of 29 free parameters: 1 for the Collins-Soper kernel, 10 for the TMD PDF, 9 for the TMD FF in pions, and 9 for the TMD FF in kaons.

JHEP08(2024)232

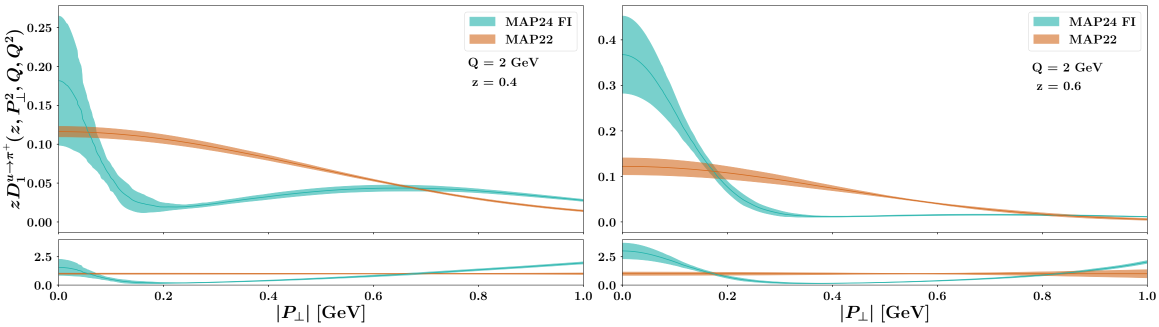

Figure 5. Comparison between the TMD FFs for an up quark fragmenting into a π^+ extracted in the MAPTMD22 fit (brown) and the MAPTMD24 Flavor Independent fit (light blue), as functions of the partonic transverse momentum $|\boldsymbol{P}_\perp|$ at $\mu = \sqrt{\zeta} = Q = 2\,\text{GeV}$ $z = 0.4$ (left panel), and $z = 0.6$ (right panel). Lower panels show the ratio of MAPTMD24 Flavor Independent to MAPTMD22. The uncertainty bands represent the 68% C.L.

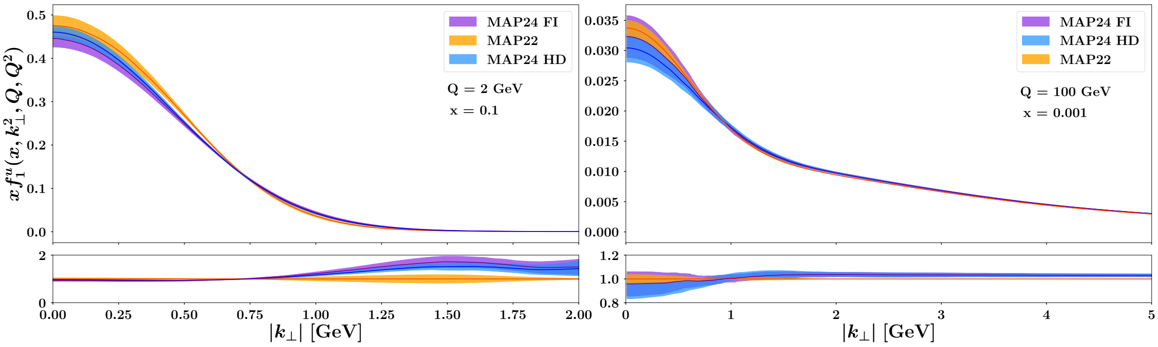

Figure 6. Comparison between the TMD PDFs of the up quark in a proton extracted in the MAPTMD22 fit (orange), the MAPTMD24 FI fit (purple) and the MAPTMD24 HD fit (blue), as functions of the partonic transverse momentum $|\boldsymbol{k}_\perp|$ at $\mu = \sqrt{\zeta} = Q = 2\,\text{GeV}$ and $x = 0.1$ (left panel), and $\mu = \sqrt{\zeta} = Q = 100\,\text{GeV}$ and $x = 0.001$ (right panel). Lower panels show the ratio of MAPTMD24 FI and MAPTMD24 HD to MAPTMD22. The uncertainty bands represent the 68% C.L.

Because of the increased flexibility, we achieve a significantly better description of the data, obtaining $\chi_0^2/N_{\text{dat}} = 1.19$ (see table 4). The SIDIS data are now described much better than in the MAPTMD24 FI case, while the description of the DY data is almost unaffected.

In figure 6, we show the unpolarized TMD PDFs of the up quark in a proton extracted in the MAPTMD22 fit (orange), the MAPTMD24 FI fit (purple) and the MAPTMD24 HD fit (blue), as functions of the partonic transverse momentum $|\boldsymbol{k}_\perp|$ at $\mu = \sqrt{\zeta} = Q = 2\,\text{GeV}$ and $x = 0.1$ (left panel), and $\mu = \sqrt{\zeta} = Q = 100\,\text{GeV}$ and $x = 0.001$ (right panel). All three extractions are compatible with each other.

In figure 7, we show the unpolarized TMD FFs for an up quark fragmenting into a π^+ in the MAPTMD22 fit (brown), the MAPTMD24 FI fit (light blue) and the MAPTMD24 HD fit (pink), as functions of the hadronic transverse momentum $|\boldsymbol{P}_\perp|$ at $\mu = \sqrt{\zeta} = Q = 2\,\text{GeV}$, and $z = 0.4$ (left panel), and $z = 0.6$ (right panel). The MAPTMD24 distributions are more strongly peaked at $|\boldsymbol{P}_\perp| = 0$ and also have a noticeable bump at higher $|\boldsymbol{P}_\perp|$ but there is a sharp difference between them, particularly at smaller values of z.

JHEP08(2024)232

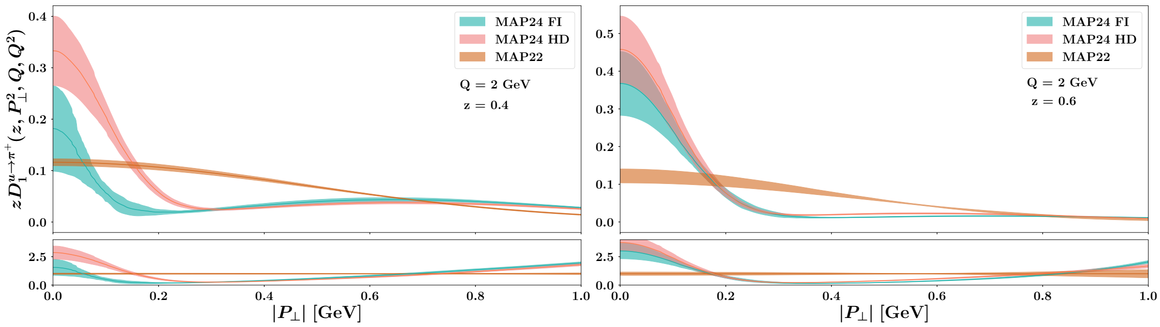

Figure 7. Comparison between the TMD FFs for an up quark fragmenting into a π^+ in the MAPTMD22 fit (brown), the MAPTMD24 FI fit (light blue) and the MAPTMD24 HD fit (pink), as functions of the hadronic transverse momentum $|\boldsymbol{P}_\perp|$ at $\mu = \sqrt{\zeta} = Q = 2\,\text{GeV}$ and $z = 0.4$ (left panel), and $z = 0.6$ (right panel). Lower panels show the ratio of MAPTMD24 FI and MAPTMD24 HD to MAPTMD22. The uncertainty bands represent the 68% C.L.

In the upper panels of figure 8, we display the unpolarized TMD FFs of the MAPTMD24 HD fit for an up quark fragmenting into a π^+ (pink) and a K^+ (blue), as functions of the hadronic transverse momentum $|\boldsymbol{P}_\perp|$ at $\mu = \sqrt{\zeta} = Q = 2\,\text{GeV}$ and $z = 0.4$ (left panel), and $z = 0.6$ (right panel). In the lower panels, we show the TMD FFs normalized to the values of the corresponding central replica at $|\boldsymbol{P}_\perp| = 0$. The lower panels clearly indicate that the fragmentations into pions and kaons exhibit distinctly different behaviors. In particular, the kaon FF displays at intermediate $|\boldsymbol{P}_\perp|$ a large second peak, emphasized at low z.

4.2 Flavor-dependent nonperturbative parametrization

In this section, we present the main result of this work, namely the extraction with a flavor-dependent approach of TMD PDFs for unpolarized quarks in the proton and TMD FFs for final pions and kaons. We will refer to this extraction as MAPTMD24 FD or simply MAPTMD24. This work represents a significant upgrade compared to the MAPTMD22 fit and similar studies, since it is the first time that a global analysis of SIDIS and DY data with flavor dependence is performed. We follow the same strategy as in the hadron-dependent extraction discussed in the previous section, i.e., we use the same functional form as in the flavor-blind case, eqs. (4.1)–(4.2), but with different parameters for different flavors. In particular, for TMD PDFs we independently parametrize the following flavors: u, $\bar{u}$, d, $\bar{d}$, and *sea*, where *sea* includes s, $\bar{s}$, c, $\bar{c}$, b, and $\bar{b}$. For simplicity, in the following the *sea* channel of TMD PDFs will be denoted as s.

For TMD FFs, we independently parametrize five different cases, as proposed in the exploratory study of ref. [30] where charge conjugation and isospin symmetries had been assumed. First, we separate the fragmentation processes where the final hadron is a pion or a kaon. Then, the fragmentation functions used to describe each process are classified as *favored* if the fragmenting quark belongs to the valence content of the final state hadron, and *unfavored* otherwise. Additionally, for the fragmentation into a K^+ we independently parametrize the favored fragmentation functions for the u and anti-strange $\bar{s}$ quarks (similarly, for K^- the favored channels involve the $\bar{u}$ and strange s quarks). In total, we have 5 sets of parameters for the following channels:

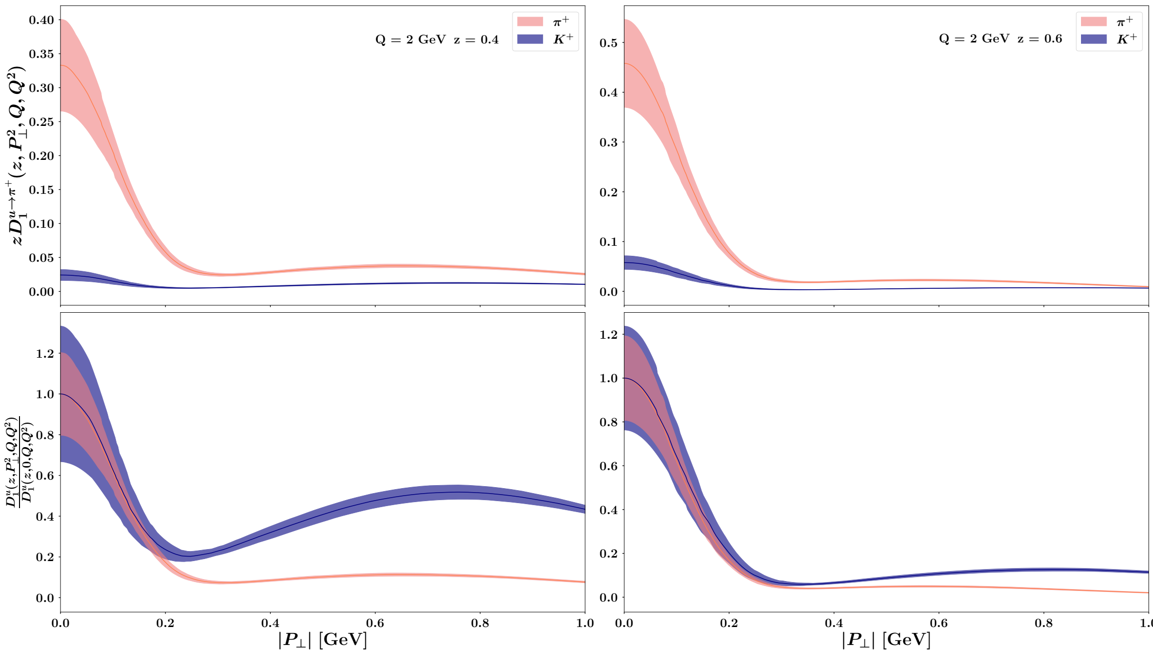

Figure 8. Comparison between the TMD FFs obtained in the MAPTMD24 HD fit for an up quark fragmenting into a π^+ (pink) and a K^+ (blue), as functions of the hadronic transverse momentum $|\boldsymbol{P}_\perp|$ at $\mu = \sqrt{\zeta} = Q = 2\,\text{GeV}$ and $z = 0.4$ (left panel), and $z = 0.6$ (right panel). In the lower panels, the TMD FFs normalized to the central replica at $|\boldsymbol{P}_\perp| = 0$. The uncertainty bands represent the 68% C.L.

- favored pion TMD FFs: $u \to \pi^+$, $d \to \pi^-$, $\bar{d} \to \pi^+$, $\bar{u} \to \pi^-$
- unfavored pion TMD FFs: $\bar{u}, d, s, \bar{s} \to \pi^+$, $u, \bar{d}, s, \bar{s} \to \pi^-$
- favored strange kaon TMD FFs: $\bar{s} \to K^+$, $s \to K^-$
- favored kaon TMD FFs: $u \to K^+$, $\bar{u} \to K^-$
- unfavored kaon TMD FFs: $\bar{u}, d, \bar{d}, s \to K^+$, $u, d, \bar{d}, \bar{s} \to K^-$.

In total, the MAPTMD24 fit involves 96 free parameters: 1 for the nonperturbative part of the Collins-Soper kernel, 50 (5 flavors $\times$10 parameters) for the nonperturbative part of the TMD PDFs, and 45 (5 channels $\times$9 parameters) for the nonperturbative part of the TMD FFs.

We fitted 100 Monte Carlo replicas of the experimental data and we obtained the global $\chi_0^2/N_{\text{dat}} = 1.08$ (see table 5), indicating that we are able to simultaneously describe the experimental data coming from both SIDIS and DY processes in an excellent way. It is noteworthy that by allowing for the possibility that flavors behave differently in transverse momentum space, we achieve a better description compared to both MAPTMD24 FI ($\chi_0^2 = 1.40$) and MAPTMD24 HD ($\chi_0^2 = 1.19$) scenarios. The description improves for both SIDIS and DY data.

We report in appendix A the plots of the comparison between experimental data and theoretical predictions for most of the included data sets, with the blue bands representing the 68% C.L. The plots show a very good agreement for all experiments.

	N^{3}LL			
Data set	$N_{\rm dat}$	χ^2_D	χ^2_λ	χ^2_0
Tevatron total	71	1.10	0.07	1.17
LHCb total	21	3.56	0.96	4.52
ATLAS total	72	3.54	0.82	4.36
CMS total	78	0.38	0.05	0.43
PHENIX 200	2	2.76	1.04	3.80
STAR 510	7	1.12	0.26	1.38
DY collider total	251	1.37	0.28	1.65
E288 200 GeV	30	0.13	0.40	0.53
E288 300 GeV	39	0.16	0.26	0.42
E288 400 GeV	61	0.11	0.08	0.19
E772	53	0.88	0.20	1.08
E605	50	0.70	0.22	0.92
DY fixed-target total	233	0.63	0.31	0.94
DY total	484	1.02	0.29	1.31
HERMES total	344	0.81	0.24	1.05
COMPASS total	1203	0.67	0.27	0.94
SIDIS total	1547	0.70	0.26	0.96
Total	**2031**	**0.81**	**0.27**	**1.08**

Table 5. Breakdown of the values of χ^2 normalized to the number of data points $N_{\rm dat}$ that survive the kinematic cuts for all datasets considered in the MAPTMD24 fit. The χ^2_D refers to uncorrelated uncertainties, χ^2_λ is the penalty term due to correlated uncertainties, χ^2_0 is the sum of χ^2_D and χ^2_λ (see text).

The values of the nonperturbative parameters and their uncertainties are reported in table 8 of appendix B. All parameters are well constrained and not compatible with zero. We observe no strong correlations among them (see figure 28 in appendix B).

4.2.1 TMDs

We now discuss the TMD PDFs and FFs extracted from the MAPTMD24 FD fit at N^{3}LL accuracy.

Figure 9 displays the unpolarized TMD PDFs for the various independent flavors, as functions of the partonic transverse momentum $|\boldsymbol{k}_\perp|$ at $\mu = \sqrt{\zeta} = Q = 2\,\text{GeV}$ and $x = 0.1$ (left panel), $x = 0.01$ (central panel), and $x = 0.001$ (right panel). The uncertainty bands represent the 68% C.L.

We note that at $x = 0.1$ the contributions of the up and down quarks dominate. The d-quark TMD PDF is larger at low values of $|\boldsymbol{k}_\perp|$ and decreases more rapidly than the u-quark one. At small x, the contributions from the sea quarks increase and become dominant at low $|\boldsymbol{k}_\perp|$ values. Furthermore, at medium to low x the $\bar{u}$-quark and $\bar{d}$-quark TMD PDFs behave in a similar way, while the u-quark and d-quark ones are very different.

JHEP08(2024)232

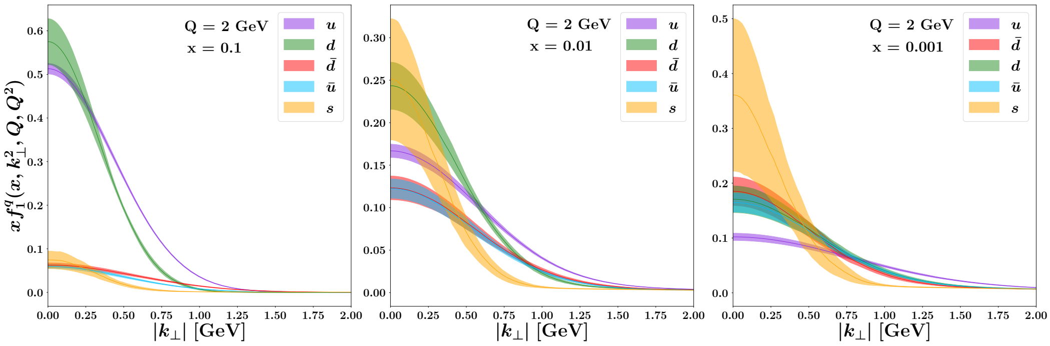

Figure 9. Comparison between the unpolarized TMD PDFs extracted in the MAPTMD24 fit with a flavor dependent approach, for a up (purple), anti-up (light blue), down (green), anti-down (red), and *sea* (orange) quark, as functions of the partonic transverse momentum $|\boldsymbol{k}_\perp|$ at $\mu = \sqrt{\zeta} = Q = 2\,\text{GeV}$ and $x = 0.1$ (left panel), $x = 0.01$ (central panel), and $x = 0.001$ (right panel). The uncertainty bands represent the 68% C.L.

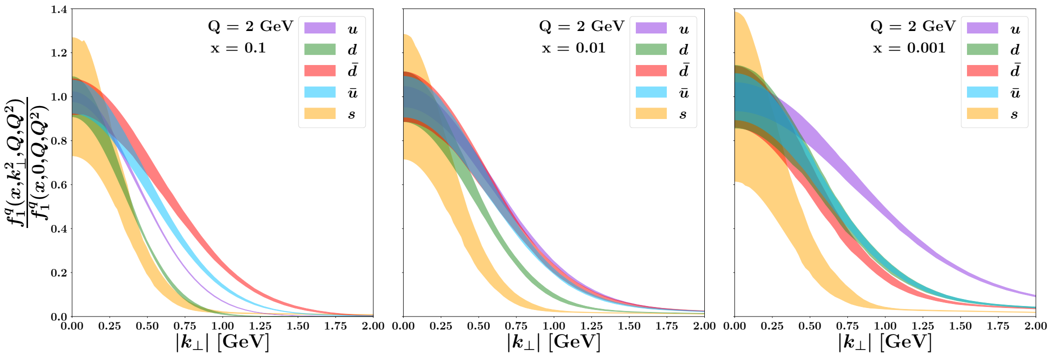

Figure 10. Comparison between the normalized unpolarized TMD PDFs extracted in the MAPTMD24 fit with a flavor-dependent approach, for a up (purple), anti-up (light blue), down (green), anti-down (red), and *sea* (orange) quark, as functions of the partonic transverse momentum $|\boldsymbol{k}_\perp|$ at $\mu = \sqrt{\zeta} = Q = 2\,\text{GeV}$ and $x = 0.1$ (left panel), $x = 0.01$ (central panel), and $x = 0.001$ (right panel). The uncertainty bands represent the 68% C.L.

In figure 10, using the same notation as above, we show the normalized TMD PDFs, i.e., divided by the value of the corresponding central replica at $|\boldsymbol{k}_\perp| = 0$. This representation allows one to better visualize the difference in shape among various flavors.

At $x = 0.1$ (left panel), the TMD PDFs of the *sea* (s) and d quarks show the sharpest decrease in $|\boldsymbol{k}_\perp|$, while the $\bar{d}$ quark is the widest. At $x = 0.001$, the s quark is still narrow, while the u quark is the widest. As x becomes smaller, the TMD PDFs of u and d become much wider while there are no significant differences in the other TMD PDFs.

Moreover, the distribution of quarks not belonging to the valence content of the proton appears to be the least constrained with large uncertainty bands for all x values, as expected from the lack of experimental data directly sensitive to sea quarks. On the contrary, at larger x (left panel) the uncertainty bands of the TMD PDFs for up and down quarks are very narrow, due to the large amount of SIDIS data in combination with high-precision DY data. It is useful to remark that the uncertainties for all flavors increase as x decreases, confirming the need for experimental data in this kinematic region.

JHEP08(2024)232

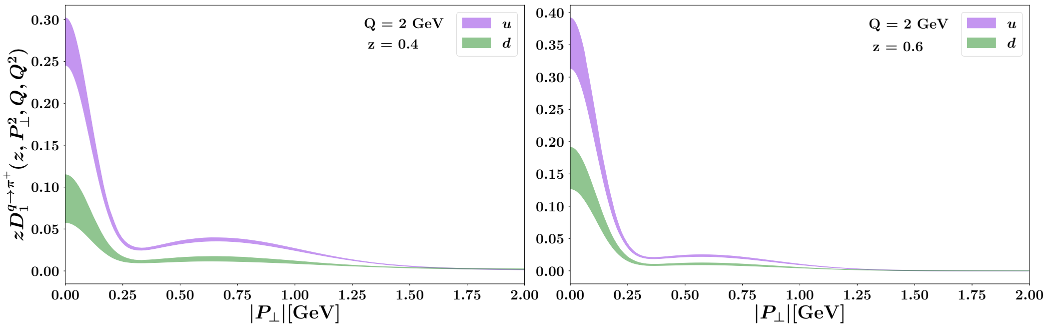

Figure 11. Comparison between the unpolarized TMD FFs for the fragmentation into a π^+ of up (purple) and down (green) quarks, extracted in the MAPTMD24 fit with a flavor dependent approach, as functions of the hadronic transverse momentum $|\boldsymbol{P}_\perp|$ at $\mu = \sqrt{\zeta} = Q = 2\,\text{GeV}$ and $z = 0.4$ (left panel), and $z = 0.6$ (right panel). The uncertainty bands represent the 68% C.L.

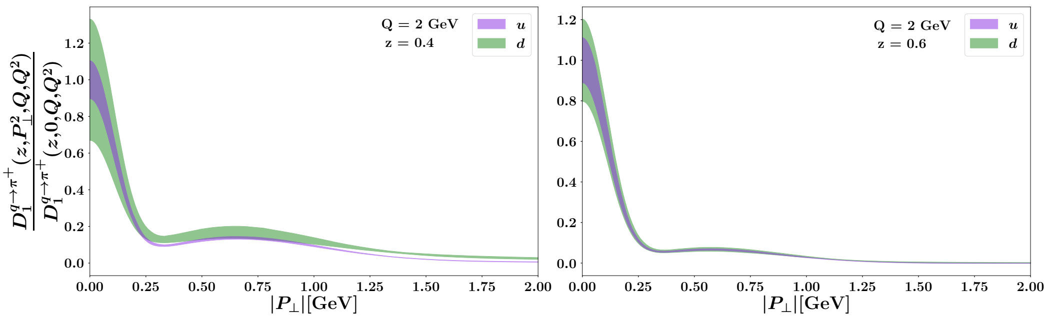

Figure 12. Comparison between the normalized unpolarized TMD FFs for the fragmentation into a π^+ of up (purple) and down (green) quarks, extracted in the MAPTMD24 fit with a flavor dependent approach, in the same conditions and with same notation as in the previous figure.

In figure 11, we display the unpolarized TMD FFs for the fragmentation into a π^+ of up (purple) and down (green) quarks, as functions of the hadronic transverse momentum $|\boldsymbol{P}_\perp|$ at $\mu = \sqrt{\zeta} = Q = 2\,\text{GeV}$ and $z = 0.4$ (left panel), and $z = 0.6$ (right panel). We note that the favored fragmentation channel (in this example, $u \to \pi^+$) dominates over the unfavored one. Also, both TMD FFs show a second bump at intermediate $|\boldsymbol{P}_\perp|$ which decreases in size at larger z, as already observed in section 4.1.

In figure 12, we display the same TMD FFs of the previous figure but normalized to each corresponding central replica at $|\boldsymbol{P}_\perp| = 0$. The unfavored channel (here, $d \to \pi^+$) is affected by larger error bands. This is mainly due to the larger uncertainties in the corresponding collinear FFs. There is generally no significant difference between favored and unfavored channels at high z, probably due to the limited sensitivity of SIDIS data in that kinematic region.

In figure 13, we show the unpolarized TMD FFs for the fragmentation of quarks u, d, and $\bar{s}$ into a K^+ in the same kinematic regions and with same conventions as in figure 11. Similarly, in figure 14 we show the normalized versions, as we did in figure 12 for the fragmentation into a π^+. We note that in general the extracted TMD FFs for kaons are affected by larger uncertainties than for pions. Also, the bump at intermediate $|\boldsymbol{P}_\perp|$ is more pronounced than in the case of pions, as was also observed with the hadron-dependent MAPTMD24 HD fit

JHEP08(2024)232

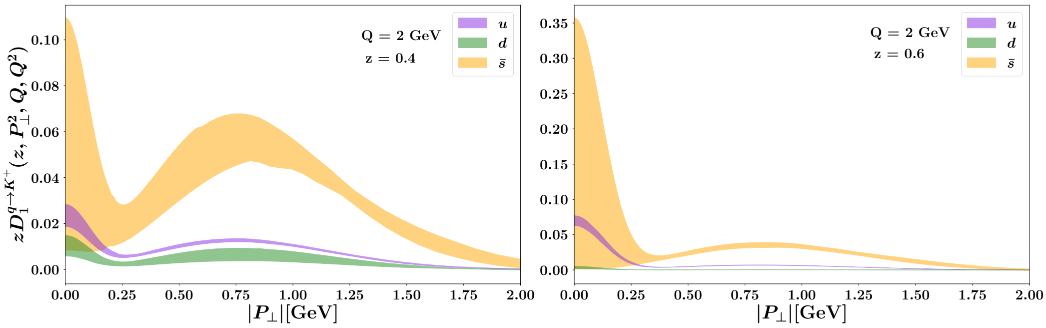

Figure 13. Comparison between the unpolarized TMD FFs for the fragmentation of up (purple), down (green), and anti-strange (orange) quarks into a K^+, extracted in the MAPTMD24 fit with a flavor dependent approach, as functions of the hadronic transverse momentum $|\boldsymbol{P}_\perp|$ at $\mu = \sqrt{\zeta} = Q = 2\,\text{GeV}$ and $z = 0.4$ (left panel), and $z = 0.6$ (right panel). The uncertainty bands represent the 68% C.L.

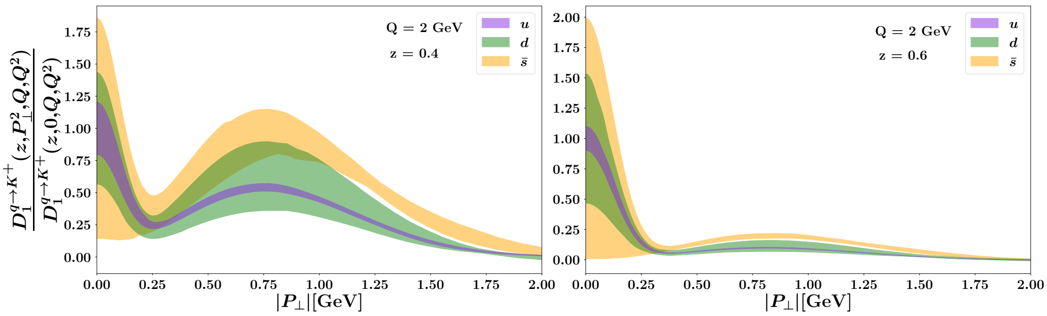

Figure 14. Comparison between the normalized unpolarized TMD FFs for the fragmentation of up (purple), down (green), and anti-strange (orange) quarks into a K^+, extracted in the MAPTMD24 fit with a flavor dependent approach, in the same kinematic conditions and with same notation as in the previous figure.

(see figure 8). Due to the size of the corresponding collinear FFs, the fragmentation channel $\bar{s} \to K^+$ is dominant, also in the normalized case. An interesting feature of our extraction is that the two favored channels ($u \to K^+$ and $\bar{s} \to K^+$) are quite different from each other. The large uncertainties in the $\bar{s} \to K^+$ fragmentation channel may be related to the fact that this TMD FF appears in the SIDIS cross section through the convolution with a TMD PDF of a *sea* quark, which is small and has large uncertainties in our extraction.

4.2.2 Impact of PDF uncertainties

In figures 20–27 of appendix A, we note that the uncertainty bands of the MAPTMD24 FD predictions are larger than those from the MAPTMD22 fit, as it can be realized by inspecting the corresponding figures 4–11 of ref. [7]. This is due to a more flexible parametrization but also to the fact that for MAPTMD24 we consider different members of collinear PDF and FF Monte Carlo sets for each TMD replica. In fact, also the error bands of the MAPTMD24 FI fit are larger than in MAPTMD22, even though the fitting function is the same. Hence, in MAPTMD24 we have a more accurate assessment of the uncertainty in the normalization of our predictions. For a better visualization of this effect, in the following we show the

JHEP08(2024)232

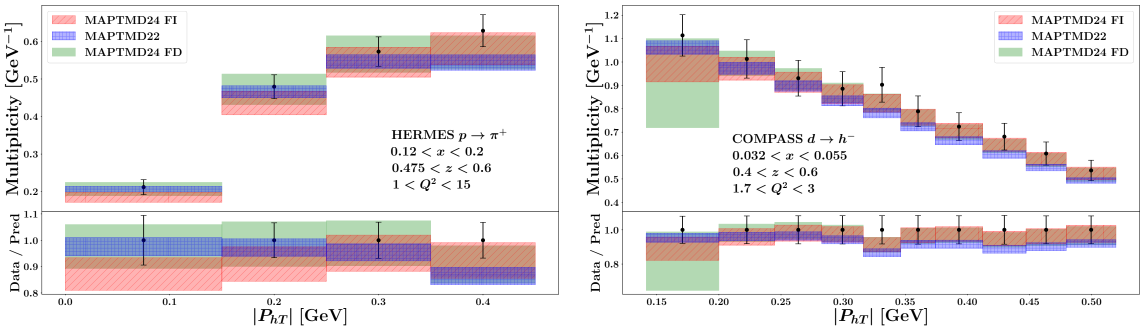

Figure 15. Comparison of SIDIS multiplicities as function of $|\boldsymbol{P}_{hT}|$, obtained by MAPTMD22 (blue), MAPTMD24 FI (green) and MAPTMD24 FD (red) fits and measured by the HERMES collaboration for π^+ off proton in the $0.12 < x < 0.2$, $0.475 < z < 0.6$, $1 < Q^2 < 15\,\mathrm{GeV}^2$ bin (left plot) and by the COMPASS collaboration for negative charged hadrons off deuteron in the $0.032 < x < 0.055$, $0.4 < z < 0.6$, $1.7 < Q^2 < 3\,\mathrm{GeV}^2$ bin (right plot). Error bands at 68% C.L.

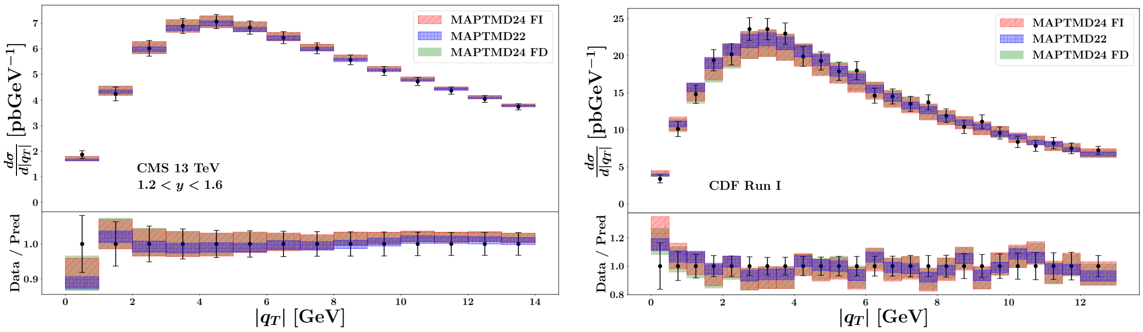

Figure 16. Same as in the previous figure but for the DY unpolarized cross section as function of $|\boldsymbol{q}_T|$, measured by the CMS collaboration at 13 TeV in the $1.2 < y < 1.6$ bin (left plot) and by the CDF collaboration in Run I (right plot).

comparison with data of the results from the MAPTMD22 (blue), MAPTMD24 FI (green) and MAPTMD24 FD (red) fits for selected bins of the SIDIS multiplicities and DY cross sections.

In figure 15, we show the comparison between both the MAPTMD24 FI and MAPTMD24 FD fits and our previous MAPTMD22 fit for the SIDIS multiplicity as function of $|\boldsymbol{P}_{hT}|$, measured by the HERMES collaboration for π^+ production off proton target in the $0.12 < x < 0.2$, $0.475 < z < 0.6$, $1 < Q^2 < 15\,\mathrm{GeV}^2$ bin (left plot), and by the COMPASS collaboration for negative charged hadrons off deuteron in the $0.032 < x < 0.055$, $0.4 < z < 0.6$, $1.7 < Q^2 < 3\,\mathrm{GeV}^2$ bin (right plot). The error bands (all at 68% C.L.) of the MAPTMD24 fits are evidently larger than the MAPTMD22 ones, and give a more accurate estimate of the uncertainty on this observable.

In figure 16, we show the same comparison as in previous figure but for the DY unpolarized cross section as function of $|\boldsymbol{q}_T|$, measured by the CMS collaboration at 13 TeV in the $1.2 < y < 1.6$ bin (left plot) and by the CDF collaboration in Run I (right plot). As for the width of the error bands, the same previous comment applies. It is also worth noting that for the DY process the MAPTMD24 FD uncertainties are very similar to the MAPTMD24 FI ones: the DY observables, being related to the sum upon all flavors of quark-antiquark contributions, are not significantly affected by the flavor dependence.

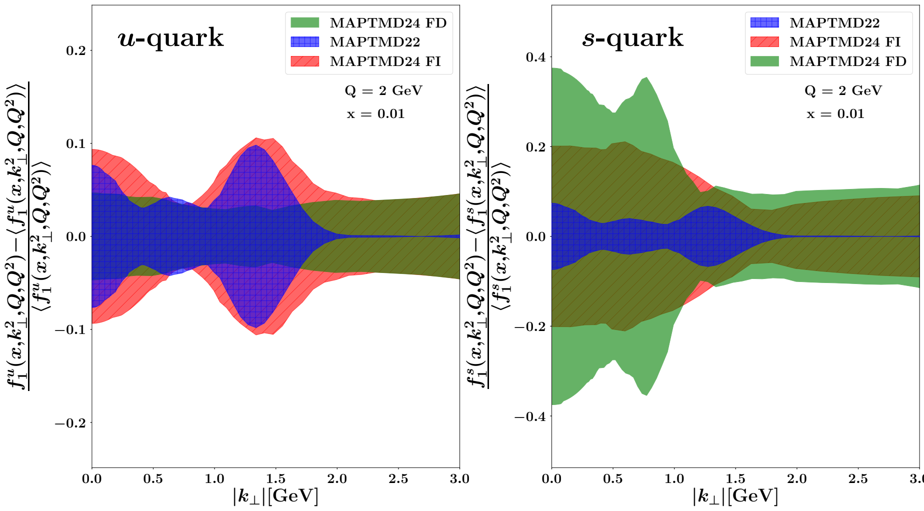

Figure 17. Comparison among the relative uncertainties of the MAPTMD24 FI (green), MAPTMD24 FD (red), MAPTMD22 (blue) fits for the up quark (left panel) and *sea* (right panel), as functions of the partonic transverse momentum $|\boldsymbol{k}_\perp|$ at $\mu = \sqrt{\zeta} = Q = 2\,\text{GeV}$ and $x = 0.01$. The uncertainty bands represent the 68% C.L.

It is useful to perform the same comparison at the level of the extracted TMDs. In figure 17, we compare the error bands at 68% C.L. of the TMD PDFs for the u quark (left plot) and *sea* (s) quark (right plot), extracted from the MAPTMD24 FI (green), MAPTMD24 FD (red), and MAPTMD22 (blue) fits. The uncertainties are relative to the corresponding average value of all fit replicas and are plotted as functions of $|\boldsymbol{k}_\perp|$ at $Q = 2\,\text{GeV}$ and $x = 0.01$. For the u quark, the error bands are similar in the low-$|\boldsymbol{k}_\perp|$ region, but at high $|\boldsymbol{k}_\perp|$ the MAPTMD24 uncertainties are larger because each TMD replica is matched onto a different replica of the collinear PDFs. For the s quark, the MAPTMD24 error bands are larger than MAPTMD22 over the whole $|\boldsymbol{k}_\perp|$ range, due to the large uncertainties in the collinear PDFs which affect both the integral of the TMD and its large $|\boldsymbol{k}_\perp|$ tail.

4.2.3 Collins-Soper kernel

In figure 18, we show the result for the Collins-Soper (CS) kernel obtained in our MAPTMD24 extraction at N^{3}LL with a flavor-dependent approach, compared to our previous MAPTMD22 results. The form of the CS kernel at low values of $|\boldsymbol{b}_T|$ is unchanged, as it depends on perturbative ingredients. The behavior at high $|\boldsymbol{b}_T|$ is determined by the combination of the b_* prescription and the parametrization of the nonperturbative component of TMD evolution in eq. (4.5).

In our new MAPTMD24 extraction, the value of the parameter g_2 is smaller than in MAPTMD22: it is approximately 0.12, about half as big as the MAPTMD22 result (≈ 0.25). Because of this difference, the new MAPTMD24 CS kernel is flatter than the MAPTMD22 one. This feature is not related to the flavor dependence of the new extraction, because it is present also in the MAPTMD24 FI and MAPTMD24 HD scenarios. Instead, it is due to the differences in the perturbative ingredients between the present work and the MAPTMD22

JHEP08(2024)232

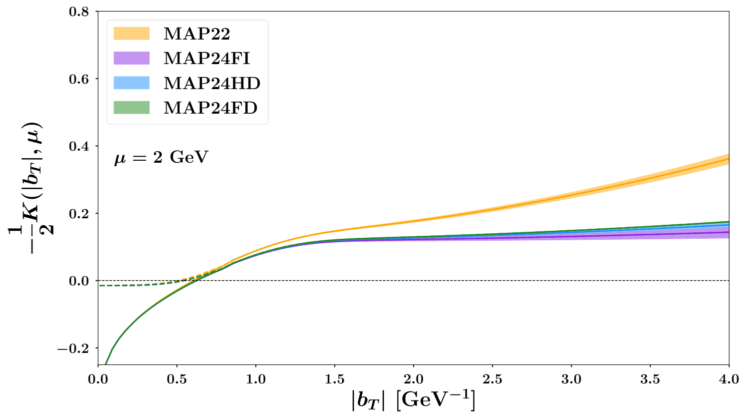

Figure 18. The Collins-Soper kernel as a function of $|\boldsymbol{b}_T|$ at the scale $\mu = 2\,\text{GeV}$ from the three versions of the present analysis (MAPTMD24 FI, MAPTMD24 HD, and MAPTMD24 FD), compared with the MAPTMD22 result [7]. The uncertainty bands represent the 68% C.L. Dashed lines show the effect of including the b_{min}-prescription of eq. (2.20).

analysis, already discussed in section 2.3. A milder dependence on $|\boldsymbol{b}_T|$ is obtained also by assuming in eq. (4.5) a constant or a linear dependence of the CS kernel on $|\boldsymbol{b}_T|$ [95–97].

The size of the error band on the CS kernel is small and similar to the MAPTMD22 one. It is possible that our fit procedure leads to an underestimation of the errors, especially for the CS kernel, since its functional form is particularly rigid and determined by a single parameter (see eq. (4.5)).

Our result can be compared with other recent extractions in the literature. The ART23 extraction [8] included DY data only and obtained a CS kernel similar to the MAPTMD22, which is therefore steeper than our MAPTMD24 result. Ref. [98] obtained a result, based on a smaller set of DY data and a simplified analysis, with larger error bands that are compatible with MAPTMD22, ART23 and also MAPTMD24. The result of ref. [99], obtained with DY data only, is also compatible with MAPTMD22 and ART23, and about 1.5 sigma away from our present results.

Apart from data-driven extractions, there have been several computations of the CS kernel in lattice QCD [100–112]. The error bars are still relatively large and there are sizeable differences between different computations. Our MAPTMD24 extraction is compatible with the recent work of ref. [112].

4.2.4 Average squared transverse momenta

In order to measure the effective width of the TMDs, in this section we study their average squared transverse momentum at specific values of x and $\mu = \sqrt{\zeta} = Q$, defined as [113, 114]:

$$\langle \boldsymbol{k}_\perp^2 \rangle^q(x, Q) = \frac{\int d^2\boldsymbol{k}_\perp\, \boldsymbol{k}_\perp^2\, f_1^q(x, \boldsymbol{k}_\perp^2, Q, Q^2)}{\int d^2\boldsymbol{k}_\perp\, f_1^q(x, \boldsymbol{k}_\perp^2, Q, Q^2)} = \frac{2M^2\, \hat{f}_1^{q\,(1)}(x, |\boldsymbol{b}_T|, Q, Q^2)}{\hat{f}_1^q(x, |\boldsymbol{b}_T|, Q, Q^2)}\Bigg|_{|\boldsymbol{b}_T|=0}, \tag{4.6}$$

where the Fourier transform $\hat{f}_1^q$ of the TMD PDF has been defined in eq. (2.6), and the first Bessel moment of the TMD PDF $\hat{f}_1^{q\,(1)}$ is defined as [113]:

$$\hat{f}_1^{q\,(1)}(x, |\boldsymbol{b}_T|, Q, Q^2) = \frac{2\pi}{M^2}\int_0^{+\infty} d|\boldsymbol{k}_\perp|\,\frac{\boldsymbol{k}_\perp^2}{|\boldsymbol{b}_T|}\,J_1\left(|\boldsymbol{k}_\perp||\boldsymbol{b}_T|\right)\,f_1^q(x, \boldsymbol{k}_\perp^2, Q, Q^2) = -\frac{2}{M^2}\frac{\partial}{\partial \boldsymbol{b}_T^2}\hat{f}_1^q(x, |\boldsymbol{b}_T|, Q, Q^2)\,. \tag{4.7}$$

As discussed in ref. [7], we shift the value of $|\boldsymbol{b}_T|$ in eq. (4.6) from 0 to $|\boldsymbol{b}_T| = 2.0\, b_{\max}$, a value well inside the nonperturbative region [114], that ensures meaningful values for the average squared transverse momenta that must be finite, positive across all the x and Q values considered in this fit, and dominated by the small-$|\boldsymbol{k}_\perp|$ region of the TMDs:

$$\langle \boldsymbol{k}_\perp^2\rangle_r^q(x, Q) = \left.\frac{2M^2\,\hat{f}_1^{q\,(1)}(x, |\boldsymbol{b}_T|, Q, Q^2)}{\hat{f}_1^q(x, |\boldsymbol{b}_T|, Q, Q^2)}\right|_{|\boldsymbol{b}_T|=2.0\,b_{\max}}, \tag{4.8}$$

where we denote with the subscript r the *regularized* definition of the average squared momenta.

The same arguments can be applied to the *regularized* average squared transverse momentum produced in the fragmentation of a given quark q into the final state hadron h [7, 44, 113, 114]:

$$\langle \boldsymbol{P}_\perp^2\rangle_r^{q\to h}(z, Q) = \left.\frac{2\,z^2\,M_h^2\,\hat{D}_1^{q\to h\,(1)}(z, |\boldsymbol{b}_T|, Q, Q^2)}{\hat{D}_1^{q\to h}(z, |\boldsymbol{b}_T|, Q, Q^2)}\right|_{|\boldsymbol{b}_T|=2.0\,b_{\max}}, \tag{4.9}$$

where the Fourier transform $\hat{D}_1^{q\to h}$ of the TMD FF is defined in eq. (2.13), and the first Bessel moment of the TMD FF $\hat{D}_1^{q\to h\,(1)}$ is defined as [44]:

$$\begin{aligned}\hat{D}_1^{q\to h\,(1)}(z, |\boldsymbol{b}_T|, Q, Q^2) &= \frac{2\pi}{M_h^2}\int_0^{+\infty}\frac{d|\boldsymbol{P}_\perp|}{z}\,\frac{|\boldsymbol{P}_\perp|}{z}\,\frac{|\boldsymbol{P}_\perp|}{z|\boldsymbol{b}_T|}\,J_1\left(|\boldsymbol{b}_T||\boldsymbol{P}_\perp|/z\right)\,D_1^{q\to h}(z, \boldsymbol{P}_\perp^2, Q, Q^2)\\ &= -\frac{2}{M_h^2}\frac{\partial}{\partial \boldsymbol{b}_T^2}\hat{D}_1^{q\to h}(z, |\boldsymbol{b}_T|, Q, Q^2)\,.\end{aligned} \tag{4.10}$$

In figure 19, we display the scatter plot of $\langle \boldsymbol{P}_\perp^2\rangle_r^{q\to h}$ at $z = 0.5$ versus $\langle \boldsymbol{k}_\perp^2\rangle_r^q$ for different flavors q. Lower panels show the results at $Q = 1\,\text{GeV}$, the upper-right panel at $Q = 5\,\text{GeV}$. The $\langle \boldsymbol{k}_\perp^2\rangle_r^q$ in the right panels are evaluated at $x = 0.1$, while in the left panel at $x = 0.001$. In the upper-left corner we display the legend of the various scatter plots with different color codes for the different flavors: the circles refer to $\langle \boldsymbol{P}_\perp^2\rangle_r^{q\to\pi^+}$ for the fragmentation into π^+ pions, while the triangles are for $\langle \boldsymbol{P}_\perp^2\rangle_r^{q\to K^+}$ into K^+ kaons. The black squares refer to the mean value of each cluster of colored points. We display only the 68% C.L. of the different ensembles of replicas.

The pink cluster, representing the replicas of the MAPTMD24 FI fit, appears along the x axis in an intermediate position with respect to other clusters, indicating that the nonperturbative component of the TMD PDFs in the flavor-independent approach is approximately an average across different flavors. Similarly, its position along the y axis is an average between the positions of the clusters of pions and kaons. The clusters for the fragmentation into kaons appear at higher average squared transverse momenta than for pions, and are more spread. For different values of x, the ordering of the various flavors changes. All these features reflect the results of the MAPTMD24 FD fit that we already commented, in particular the outcome in figure 10. Finally, both the values of $\langle \boldsymbol{k}_\perp^2\rangle_r^q$ and $\langle \boldsymbol{P}_\perp^2\rangle_r^{q\to h}$ increase as Q increases, since

JHEP08(2024)232

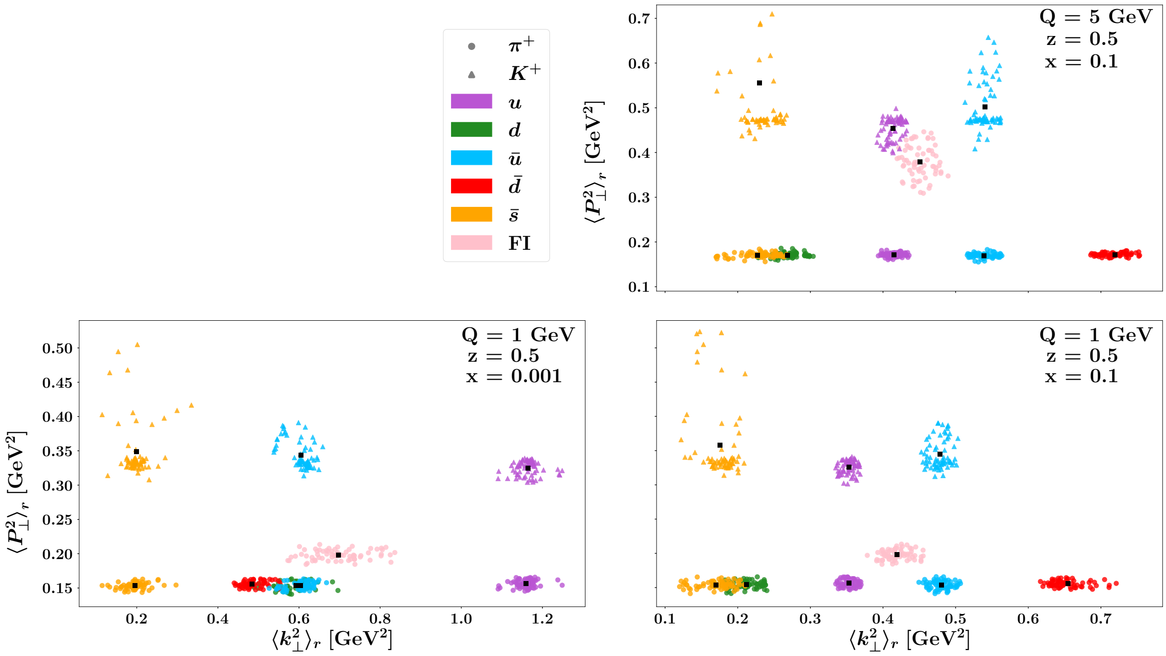

Figure 19. Scatter plot of average squared transverse momenta for the unpolarized TMD PDF at $x = 0.1$ (right panels), $x = 0.001$ (left panel) and for the unpolarized TMD FF for fragmentation into π^+ (circle) or into K^+ (triangle) at $z = 0.5$. In the upper panel, TMDs are evaluated at $Q = 5\,\text{GeV}$, in the lower panels at $Q = 1\,\text{GeV}$. Different colors for different flavors as indicated in the legend. Black squares represent the mean value for the different clusters. The 68% C.L. of the different ensembles of replicas is reported.

the evolution equations generate a broadening of the transverse momentum distributions. A similar trend is observed also in parton-shower-based Monte Carlo generators of collider events, either after underlying-event tuning [115] or after including TMD effects into the shower according to the parton branching model [116].

5 Conclusions

In this paper, we performed an extraction of transverse-momentum-dependent parton distribution and fragmentation functions from a comprehensive set of 2031 experimental data points from the Drell-Yan (DY) process and semi-inclusive deep-inelastic scattering (SIDIS), with the main goal of unraveling the distinctions among different quark flavors. It is the first time that the flavor-dependent nature of Transverse Momentum Distributions (TMDs) is fully taken into consideration in a global fit.

Our study builds upon previous work by incorporating state-of-the-art theory results reaching N^{3}LL accuracy, and adopting the fitting framework used in our past works, available through the `NangaParbat` public code.[4] As done in ref. [6] for DY, we used Monte Carlo replicas of collinear PDFs and FFs. This enabled an accurate portrayal of the flavor-specific characteristics of TMDs and their uncertainties, at least within the choices for prescriptions and functional forms that we adopted.

[4]The code and a collection of final results will be made publicly available by the MAP collaboration at https://github.com/MapCollaboration.

JHEP08(2024)232

After reviewing the formalism in section 2 and the analysis framework in section 3, we presented three extractions with three different approaches. In section 4.1, we discussed a Flavor Independent extraction (MAPTMD24 FI) and a Hadron Dependent one (MAPTMD24 HD), characterized by different fragmentation functions for different final-state hadrons. They constitute a baseline to assess the relevance of a flavor-depedent fit. We adopted the same choices as in our previous extraction (MAPTMD22), but we used two Monte Carlo sets of collinear PDFs and FFs in order to fully account for their uncertainties. We obtained $\chi_0^2/N_{\text{dat}} = 1.40$ and 1.19 for the two extractions, respectively.

Section 4.2 presents the core of our analysis, where we separately parametrized five TMD PDFs (u, $\bar{u}$, d, $\bar{d}$, and *sea*) and five TMD FFs (favored and unfavored pion fragmentation, favored, unfavored and s-quark kaon fragmentation). We extracted a total of 96 free parameters. This flavor-dependent extraction (MAPTMD24 FD) reached $\chi_0^2/N_{\text{dat}} = 1.08$. Therefore, the MAPTMD24 FD fit demonstrates superior capability in simultaneously describing data from both SIDIS and DY processes, and is able to capture the nontrivial interplay between quark flavors and their transverse momentum distributions.

The extracted TMD PDFs and FFs offer valuable insights into the three-dimensional structure of hadrons, revealing distinctive flavor-dependent behaviors across different kinematic regimes. In particular, the u-quark TMD PDF results to be the most constrained among all flavors, and it is the widest at small and intermediate x. On the other hand, an examination of TMD FFs demonstrates the importance of distinguishing between favored and unfavored channels, particularly evident for kaon fragmentations.

We also obtained a new determination of the Collins-Soper kernel, which provides crucial insights into TMD evolution. Our MAPTMD24 result shows a lower slope at large b_T compared to other recent results [7, 8, 98, 99]. Further precise, multidimensional data sets spanning a wide Q^2 range will be invaluable to further investigate these differences.

Overall, our study represents a significant step forward in the quest for a comprehensive understanding of the flavor-dependent structure of hadrons in momentum space. Our findings pave the way for more refined theoretical predictions and improved interpretations of experimental phenomena in high-energy physics.

Acknowledgments

We thank Emanuele Nocera for stimulating discussions. This work is supported by the European Union's Horizon 2020 programme under grant agreement No. 824093 (STRONG2020) and by the European Union "Next Generation EU" program through the Italian PRIN 2022 grant n. 20225ZHA7W. Argonne National Laboratory's work was supported by the U.S. Department of Energy, Office of Science, under the contract DE-AC02-06CH11357. This material is also based upon work supported by the U.S. Department of Energy, Office of Science, Office of Nuclear Physics under contract DE-AC05-06OR23177.

A Quality of global fit

In this appendix, we present in figures 20–27 the quality of our fit (MAPTMD24 FD) for most of the used data. The blue error bands represent the 68% C.L. of the theoretical predictions.

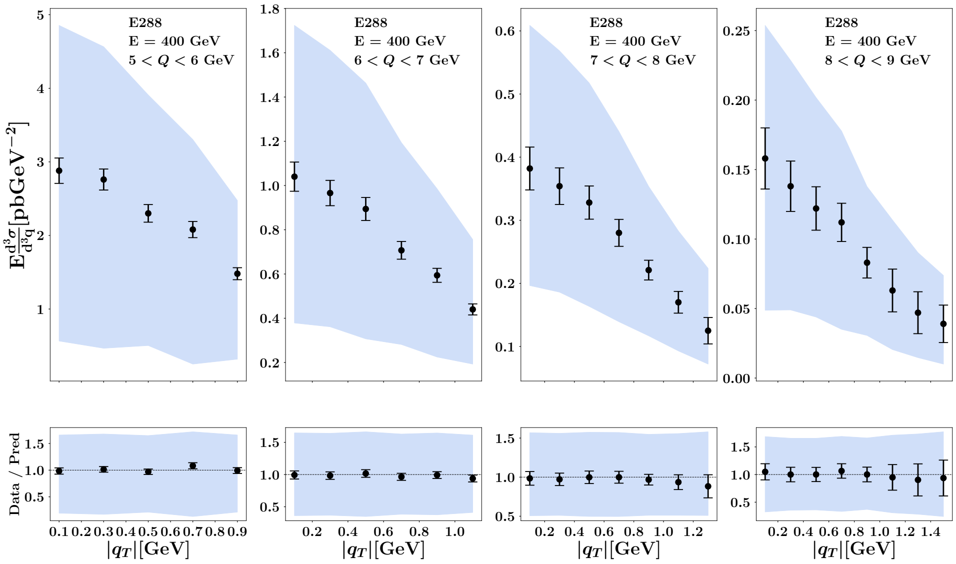

Figure 20. Upper panel: comparison between data and theoretical predictions for the DY cross section differential in $|\boldsymbol{q}_T|$ for the E288 dataset at $E_{\text{beam}} = 400\,\text{GeV}$ for different Q bins; uncertainty bands correspond to the 68% C.L. Lower panel: ratio between experimental data and theoretical cross section.

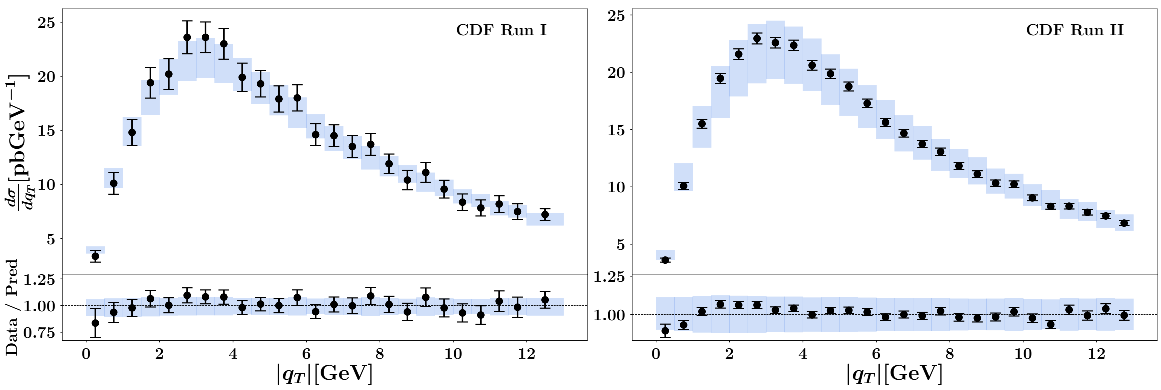

Figure 21. Upper panels: comparison between experimental data and theoretical predictions for the cross section differential in $|\boldsymbol{q}_T|$ for Z bosons produced in $p\bar{p}$ collisions at the Tevatron from CDF Run I (left panel) and run II (right panel); uncertainty bands correspond to the 68% C.L. Lower panel: ratio between experimental data and theoretical results.

JHEP08(2024)232

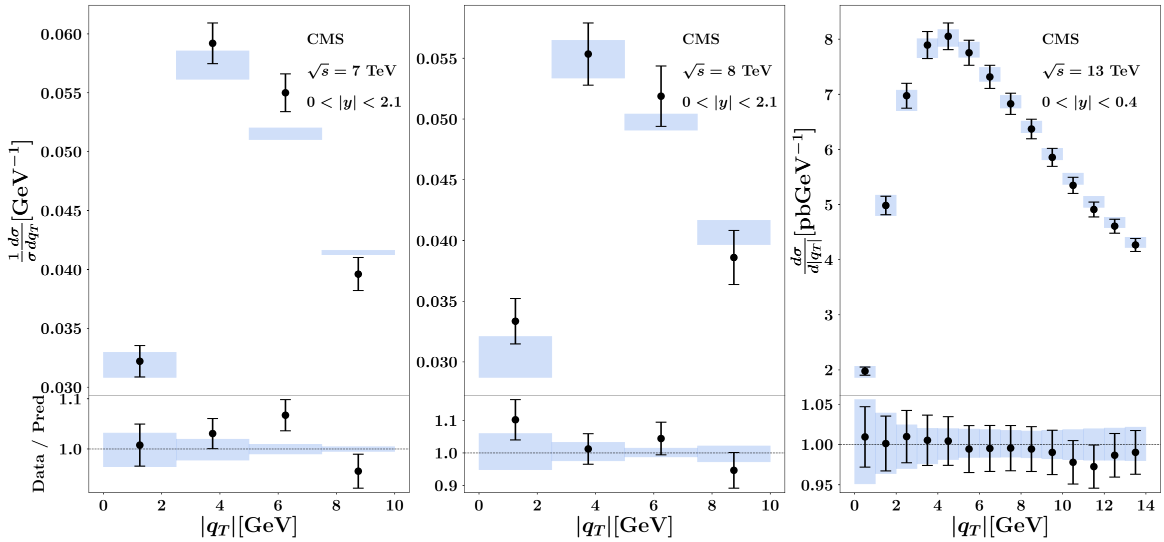

Figure 22. Same as in previous figure but for Z boson production in pp collisions measured by the CMS collaboration. From left to right: increasing $\sqrt{s} = 7,\ 8,\ 13$ TeV, respectively. For $\sqrt{s} = 7,\ 8$ TeV, the results are normalized to the fiducial cross section.

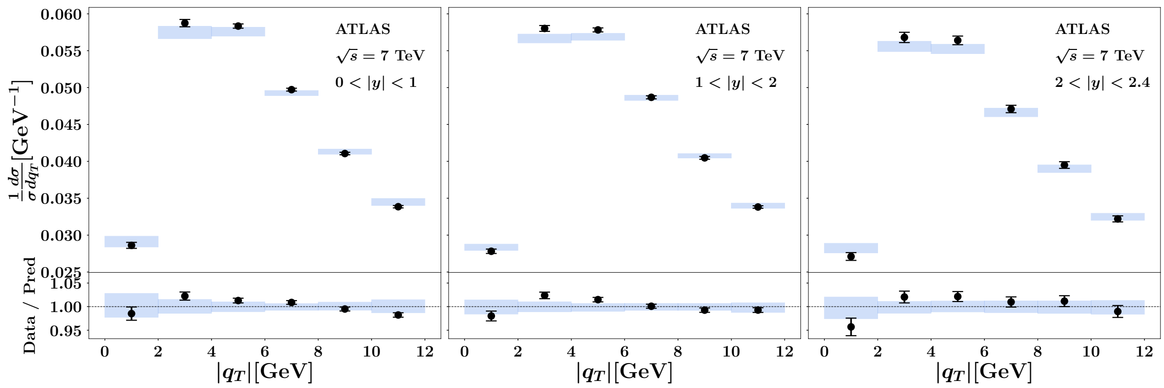

Figure 23. Same as in the left and central panels of previous figure, but for ATLAS kinematics at $\sqrt{s} = 7$ TeV. From left to right, results at increasing rapidity.

JHEP08(2024)232

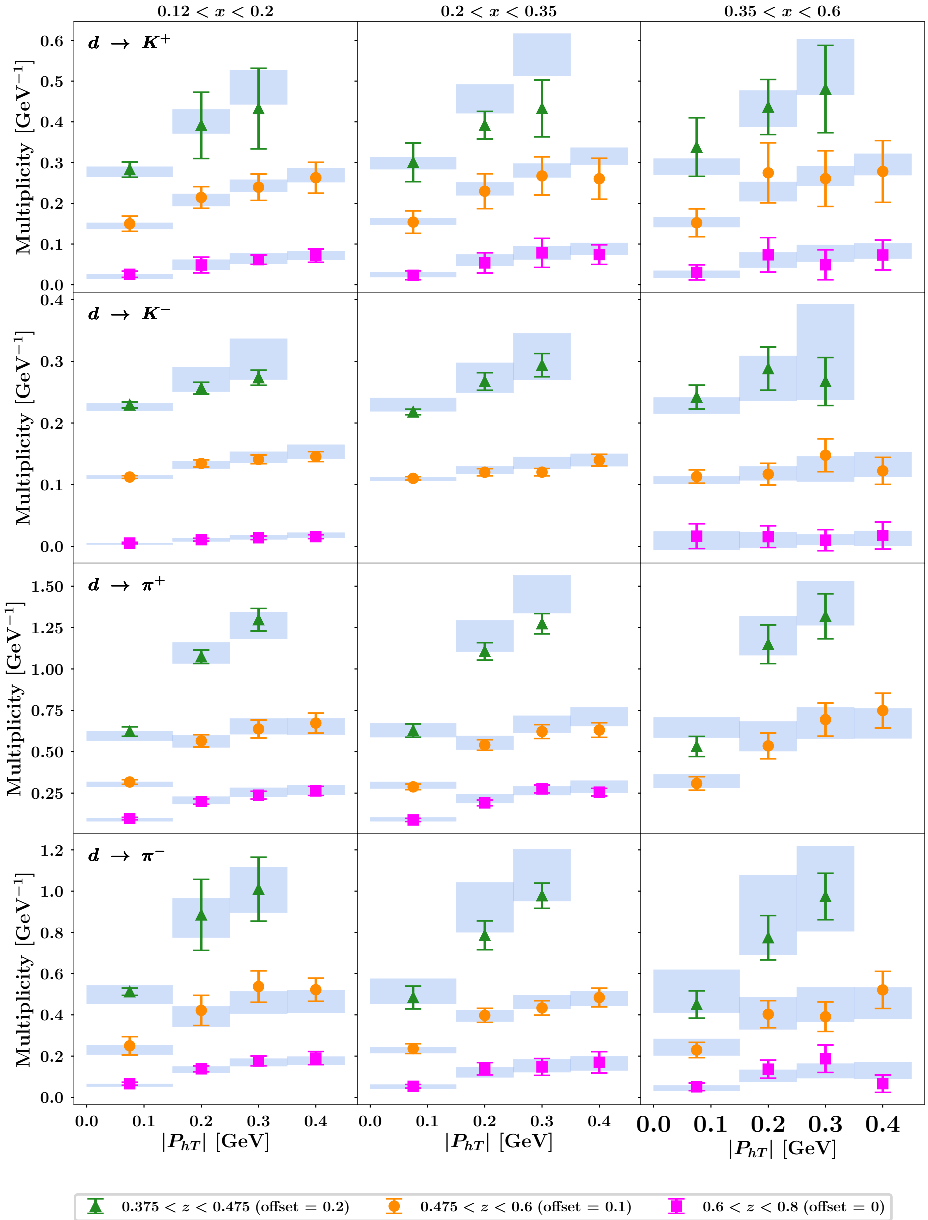

Figure 24. Comparison between data and theoretical predictions for the HERMES multiplicities for the production of charged pions and kaons off a deuteron target for different x and z bins as a function of the transverse momentum $|\boldsymbol{P}_{hT}|$ of the final-state hadron. For better visualization, each z bin is shifted by the indicated offset.

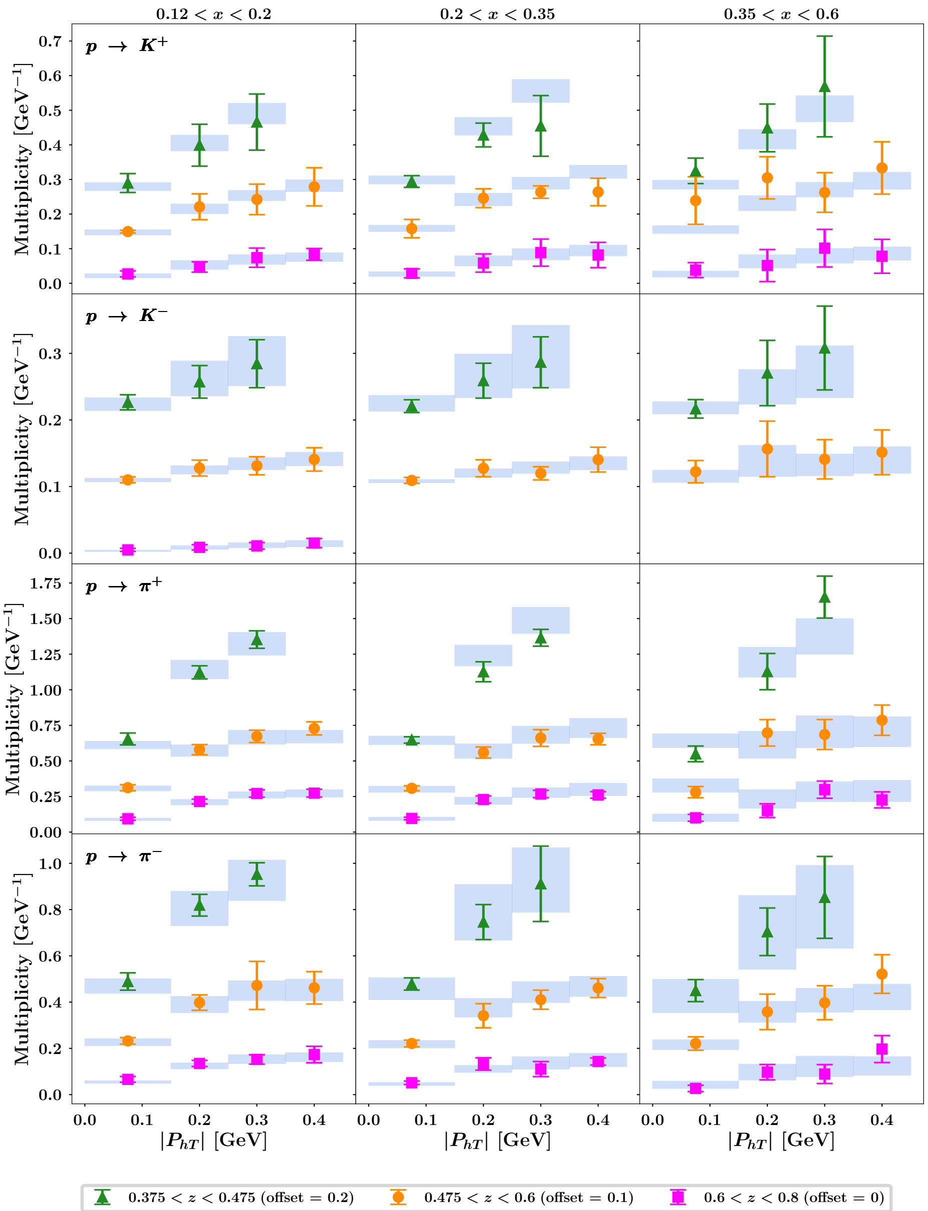

Figure 25. Comparison between data and theoretical predictions for the HERMES multiplicities for the production of charged pions and kaons off a proton target for different x and z bins as a function of the transverse momentum $|\boldsymbol{P}_{hT}|$ of the final-state hadron. For better visualization, each z bin is shifted by the indicated offset.

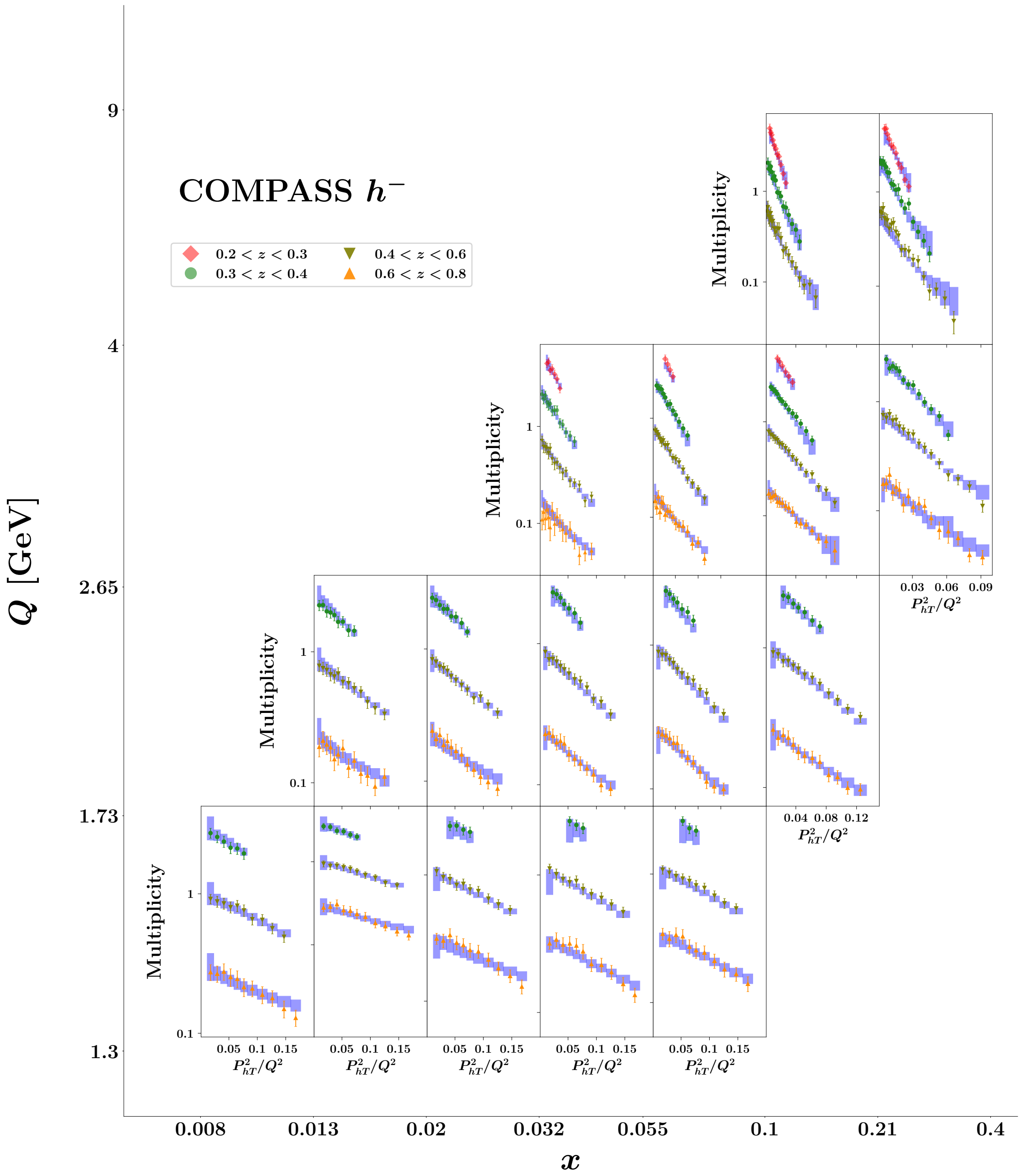

Figure 26. Comparison between data and theoretical predictions for the COMPASS multiplicities for the production of negative charged hadrons off a deuteron target. For each Q, x bin, the multiplicities are displayed as functions of $\boldsymbol{P}_{hT}^2/Q^2$ for different z bins surviving kinematic cuts, as indicated in the legend.

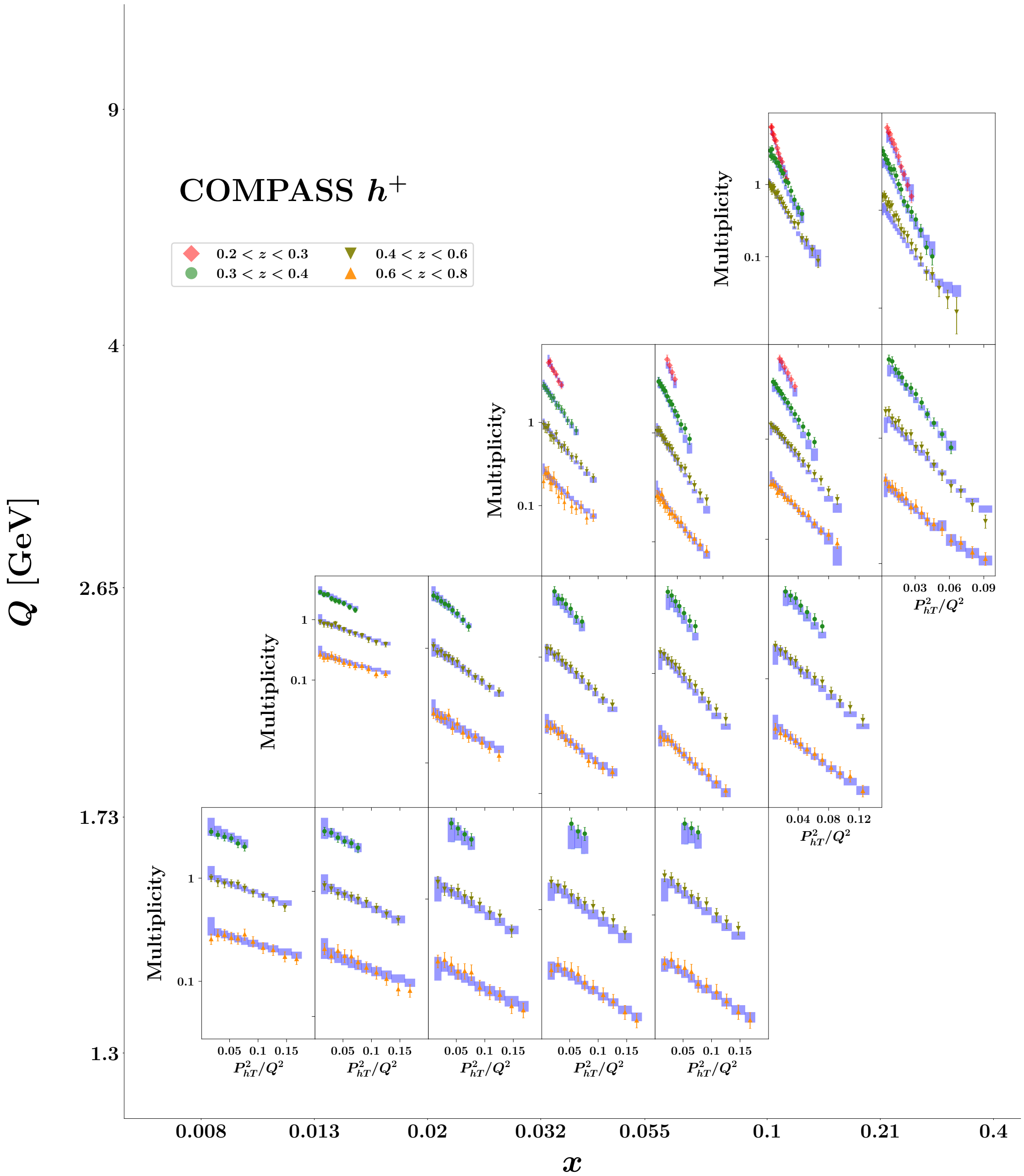

Figure 27. Same as in the previous figure but for the production of positive charged hadrons off a deuteron target.

B Nonperturbative parameters

In tables 6, 7, and 8 we report the tables with the central values of the fitted parameters for the MAPTMD24 FI, MAPTMD24 HD, and MAPTMD24 FD extractions. For the latter one, in figure 28 we also show a graphical representation of the correlation matrix.

Parameter	Average over replicas
g_2 [GeV]	0.080 ± 0.030
N_1 [GeV^2]	0.42 ± 0.022
N_2 [GeV^2]	0.022 ± 0.003
N_3 [GeV^2]	$(49 \pm 7.8) \times 10^{-5}$
α_1	0.21 ± 0.20
α_2	5.42 ± 0.074
α_3	2.27 ± 0.34
σ_1	-0.11 ± 0.03
σ_3	10.16 ± 0.34
λ_1 [GeV^{-1}]	0.48 ± 0.060
λ_2 [GeV^{-1}]	0.095 ± 0.016
N_4 [GeV^2]	$(107 \pm 6.0) \times 10^{-5}$
N_5 [GeV^2]	0.11 ± 0.0036
β_1	11.62 ± 0.22
β_2	4.34 ± 0.17
δ_1	0.0023 ± 0.0021
δ_2	0.19 ± 0.012
γ_1	1.27 ± 0.055
γ_2	0.16 ± 0.15
λ_F [GeV^{-2}]	0.16 ± 0.010

Table 6. Mean value and error related to the 68% C.L. over the Monte Carlo replicas of the free parameters in the flavor-blind MAPTMD24 FI fit.

Parameter	Average over replicas
g_2[GeV]	0.11 ± 0.016
N_1[GeV^2]	0.40 ± 0.014
N_2[GeV^2]	0.020 ± 0.0022
N_3[GeV^2]	$(3.8 \pm 1.5) \times 10^{-4}$
α_1	0.40 ± 0.24
α_2	5.4 ± 0.026
α_3	2.2 ± 0.076
σ_1	-0.12 ± 0.018
σ_3	10 ± 0.030
λ_1[GeV^{-1}]	0.48 ± 0.089
λ_2[GeV^{-1}]	0.084 ± 0.0054
$N_{4\pi}$[GeV^2]	$(85 \pm 6.0) \times 10^{-5}$
$N_{5\pi}$[GeV^2]	0.096 ± 0.0015
$\beta_{1\pi}$	5.1 ± 0.28
$\beta_{2\pi}$	2.0 ± 0.070
$\delta_{1\pi}$	0.0027 ± 0.0027
$\delta_{2\pi}$	0.19 ± 0.00075
$\gamma_{1\pi}$	1.4 ± 0.059
$\gamma_{2\pi}$	0.88 ± 0.038
$\lambda_{F\pi}$[GeV^{-2}]	0.082 ± 0.0049
N_{4K}[GeV^2]	$(72 \pm 8.8) \times 10^{-5}$
N_{5K}[GeV^2]	0.15 ± 0.0053
β_{1K}	8.5 ± 0.52
β_{2K}	3.9 ± 0.21
δ_{1K}	0.0072 ± 0.0065
δ_{2K}	0.19 ± 0.0095
γ_{1K}	1.3 ± 0.14
γ_{2K}	0.18 ± 0.15
λ_{FK}[GeV^{-2}]	0.16 ± 0.021

Table 7. Mean value and error related to the 68% C.L. over the Monte Carlo replicas of the free parameters in the hadron-dependent MAPTMD24 HD fit.

JHEP08(2024)232

Parameter	Value	Parameter	Value	Parameter	Value
g_2 [GeV]	0.12 ± 0.0033				
N_{1d} [GeV^2]	0.21 ± 0.017	N_{2d} [GeV^2]	0.015 ± 0.0013	N_{3d} [GeV^2]	$(40 \pm 2.2) \times 10^{-4}$
α_{1d}	0.86 ± 0.11	α_{2d}	5.5 ± 0.041	α_{3d}	2.38 ± 0.032
σ_{1d}	-0.21 ± 0.013	$\sigma_{2d} = \sigma_{3d}$	9.91 ± 0.061		
λ_{1d} [GeV^{-1}]	0.32 ± 0.038	λ_{2d} [GeV^{-1}]	0.052 ± 0.0022		
$N_{1\bar{d}}$ [GeV^2]	0.68 ± 0.038	$N_{2\bar{d}}$ [GeV^2]	0.0037 ± 0.0037	$N_{3\bar{d}}$ [GeV^2]	$(5.9 \pm 5.8) \times 10^{-5}$
$\alpha_{1\bar{d}}$	0.64 ± 0.18	$\alpha_{2\bar{d}}$	5.69 ± 0.64	$\alpha_{3\bar{d}}$	1.57 ± 0.53
$\sigma_{1\bar{d}}$	0.075 ± 0.012	$\sigma_{2\bar{d}} = \sigma_{3\bar{d}}$	10.19 ± 0.09		
$\lambda_{1\bar{d}}$ [GeV^{-1}]	0.7 ± 0.67	$\lambda_{2\bar{d}}$ [GeV^{-1}]	0.051 ± 0.0071		
N_{1u} [GeV^2]	0.35 ± 0.0063	N_{2u} [GeV^2]	0.019 ± 0.00015	N_{3u} [GeV^2]	$(355 \pm 4.5) \times 10^{-6}$
α_{1u}	0.18 ± 0.1	α_{2u}	5.42 ± 0.0037	α_{3u}	2.14 ± 0.0068
σ_{1u}	-0.26 ± 0.0079	$\sigma_{2u} = \sigma_{3u}$	10.17 ± 0.011		
λ_{1u} [GeV^{-1}]	0.49 ± 0.0037	λ_{2u} [GeV^{-1}]	0.081 ± 0.0009		
$N_{1\bar{u}}$ [GeV^2]	0.48 ± 0.0074	$N_{2\bar{u}}$ [GeV^2]	0.022 ± 0.00037	$N_{3\bar{u}}$ [GeV^2]	$(21 \pm 1.5) \times 10^{-5}$
$\alpha_{1\bar{u}}$	0.95 ± 0.077	$\alpha_{2\bar{u}}$	5.38 ± 0.0099	$\alpha_{3\bar{u}}$	1.77 ± 0.052
$\sigma_{1\bar{u}}$	-0.026 ± 0.01	$\sigma_{2\bar{u}} = \sigma_{3\bar{u}}$	10.21 ± 0.02		
$\lambda_{1\bar{u}}$ [GeV^{-1}]	0.53 ± 0.0067	$\lambda_{2\bar{u}}$ [GeV^{-1}]	0.11 ± 0.0055		
N_{1sea} [GeV^2]	0.16 ± 0.035	N_{2sea} [GeV^2]	0.029 ± 0.0027	N_{3sea} [GeV^2]	0.0039 ± 0.002
α_{1sea}	0.65 ± 0.48	α_{2sea}	5.24 ± 0.032	α_{3sea}	1.48 ± 0.74
σ_{1sea}	-0.018 ± 0.022	$\sigma_{2sea} = \sigma_{3sea}$	10.72 ± 0.037		
λ_{1sea} [GeV^{-1}]	2.43 ± 0.97	λ_{2sea} [GeV^{-1}]	0.015 ± 0.0083		
$N_{4u\pi}$ [GeV^2]	$(82 \pm 1.8) \times 10^{-5}$	$N_{5u\pi}$ [GeV^2]	0.095 ± 0.0008	$\beta_{1u\pi}$	5.19 ± 0.066
$\beta_{2u\pi}$	2.3 ± 0.041	$\delta_{1u\pi}$	0.017 ± 0.0084	$\delta_{2u\pi}$	0.19 ± 0.0049
$\gamma_{1u\pi}$	1.46 ± 0.015	$\gamma_{2u\pi}$	0.8 ± 0.0095	$\lambda_{Fu\pi}$ [GeV^{-2}]	0.089 ± 0.003
$N_{4sea\pi}$ [GeV^2]	$(83 \pm 2.4) \times 10^{-5}$	$N_{5sea\pi}$ [GeV^2]	0.094 ± 0.0012	$\beta_{1sea\pi}$	5.38 ± 0.21
$\beta_{2sea\pi}$	2.31 ± 0.072	$\delta_{1sea\pi}$	0.022 ± 0.0064	$\delta_{2sea\pi}$	0.19 ± 0.0044
$\gamma_{1sea\pi}$	1.44 ± 0.026	$\gamma_{2sea\pi}$	0.8 ± 0.012	$\lambda_{Fsea\pi}$ [GeV^{-2}]	0.086 ± 0.004
N_{4uK} [GeV^2]	$(87 \pm 5.7) \times 10^{-5}$	N_{5uK} [GeV^2]	0.14 ± 0.0026	β_{1uK}	8.52 ± 0.081
β_{2uK}	3.86 ± 0.19	δ_{1uK}	0.0061 ± 0.0035	δ_{2uK}	0.19 ± 0.0059
γ_{1uK}	1 ± 0.041	γ_{2uK}	0.19 ± 0.054	λ_{FuK} [GeV^{-2}]	0.14 ± 0.0048
$N_{4\bar{s}K}$ [GeV^2]	$(4.5 \pm 3.7) \times 10^{-4}$	$N_{5\bar{s}K}$ [GeV^2]	0.16 ± 0.016	$\beta_{1\bar{s}K}$	7.17 ± 1.4
$\beta_{2\bar{s}K}$	5.1 ± 1.04	$\delta_{1\bar{s}K}$	1.51 ± 1.51	$\delta_{2\bar{s}K}$	0.16 ± 0.033
$\gamma_{1\bar{s}K}$	0.71 ± 0.42	$\gamma_{2\bar{s}K}$	0.36 ± 0.19	$\lambda_{F\bar{s}K}$ [GeV^{-2}]	0.34 ± 0.2
N_{4seaK} [GeV^2]	$(78 \pm 2.8) \times 10^{-5}$	N_{5seaK} [GeV^2]	0.15 ± 0.0059	β_{1seaK}	8.63 ± 0.24
β_{2seaK}	4.19 ± 0.14	δ_{1seaK}	0.0075 ± 0.0051	δ_{2seaK}	0.2 ± 0.0029
γ_{1seaK}	0.96 ± 0.036	γ_{2seaK}	0.17 ± 0.092	λ_{FseaK} [GeV^{-2}]	0.15 ± 0.0055

Table 8. Table of the 96 free parameters in the flavor-dependent MAPTMD24 FD fit. For each parameter, the mean value and the error related to the 68% C.L. are reported.

JHEP08(2024)232

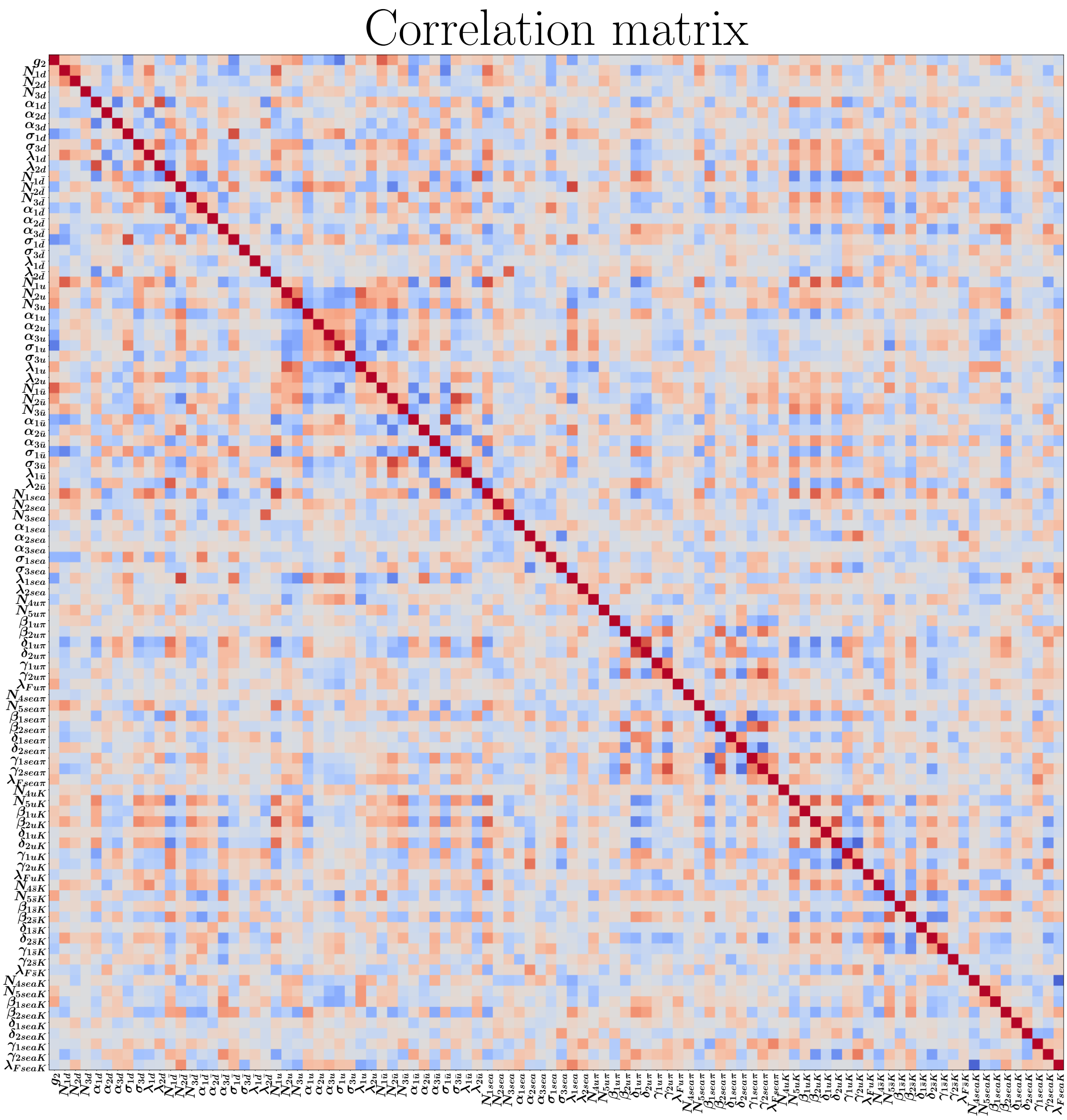

Figure 28. Graphical representation of the correlation matrix for the free parameters of the MAPTMD24 FD fit; color code ranges from blue (-1) to red ($+1$).

References

[1] A. Bacchetta, F. Delcarro, C. Pisano, M. Radici and A. Signori, *Extraction of partonic transverse momentum distributions from semi-inclusive deep-inelastic scattering, Drell-Yan and Z-boson production*, *JHEP* **06** (2017) 081 [*Erratum ibid.* **06** (2019) 051] [arXiv:1703.10157] [INSPIRE].

[2] I. Scimemi and A. Vladimirov, *Analysis of vector boson production within TMD factorization*, *Eur. Phys. J. C* **78** (2018) 89 [arXiv:1706.01473] [INSPIRE].

[3] V. Bertone, I. Scimemi and A. Vladimirov, *Extraction of unpolarized quark transverse momentum dependent parton distributions from Drell-Yan/Z-boson production*, JHEP **06** (2019) 028 [arXiv:1902.08474] [INSPIRE].

[4] I. Scimemi and A. Vladimirov, *Non-perturbative structure of semi-inclusive deep-inelastic and Drell-Yan scattering at small transverse momentum*, JHEP **06** (2020) 137 [arXiv:1912.06532] [INSPIRE].

[5] A. Bacchetta et al., *Transverse-momentum-dependent parton distributions up to N^3LL from Drell-Yan data*, JHEP **07** (2020) 117 [arXiv:1912.07550] [INSPIRE].

[6] M. Bury, F. Hautmann, S. Leal-Gomez, I. Scimemi, A. Vladimirov and P. Zurita, *PDF bias and flavor dependence in TMD distributions*, JHEP **10** (2022) 118 [arXiv:2201.07114] [INSPIRE].

[7] MAP collaboration, *Unpolarized transverse momentum distributions from a global fit of Drell-Yan and semi-inclusive deep-inelastic scattering data*, JHEP **10** (2022) 127 [arXiv:2206.07598] [INSPIRE].

[8] V. Moos, I. Scimemi, A. Vladimirov and P. Zurita, *Extraction of unpolarized transverse momentum distributions from the fit of Drell-Yan data at N^4LL*, JHEP **05** (2024) 036 [arXiv:2305.07473] [INSPIRE].

[9] A. Bermudez Martinez et al., *Collinear and TMD parton densities from fits to precision DIS measurements in the parton branching method*, Phys. Rev. D **99** (2019) 074008 [arXiv:1804.11152] [INSPIRE].

[10] A. Bermudez Martinez et al., *Production of Z-bosons in the parton branching method*, Phys. Rev. D **100** (2019) 074027 [arXiv:1906.00919] [INSPIRE].

[11] A. Bermudez Martinez et al., *The transverse momentum spectrum of low mass Drell-Yan production at next-to-leading order in the parton branching method*, Eur. Phys. J. C **80** (2020) 598 [arXiv:2001.06488] [INSPIRE].

[12] F. Hautmann et al., *TMDlib and TMDplotter: library and plotting tools for transverse-momentum-dependent parton distributions*, Eur. Phys. J. C **74** (2014) 3220 [arXiv:1408.3015] [INSPIRE].

[13] N.A. Abdulov et al., *TMDlib2 and TMDplotter: a platform for 3D hadron structure studies*, Eur. Phys. J. C **81** (2021) 752 [arXiv:2103.09741] [INSPIRE].

[14] R. Angeles-Martinez et al., *Transverse Momentum Dependent (TMD) parton distribution functions: status and prospects*, Acta Phys. Pol. B **46** (2015) 2501 [arXiv:1507.05267] [INSPIRE].

[15] J.J. Ethier and E.R. Nocera, *Parton Distributions in Nucleons and Nuclei*, Annu. Rev. Nucl. Part. Sci. **70** (2020) 43 [arXiv:2001.07722] [INSPIRE].

[16] S. Albino et al., *Parton fragmentation in the vacuum and in the medium*, arXiv:0804.2021 [INSPIRE].

[17] A. Metz and A. Vossen, *Parton Fragmentation Functions*, Prog. Part. Nucl. Phys. **91** (2016) 136 [arXiv:1607.02521] [INSPIRE].

[18] M. Burkardt and B. Pasquini, *Modelling the nucleon structure*, Eur. Phys. J. A **52** (2016) 161 [arXiv:1510.02567] [INSPIRE].

[19] A. Bacchetta, F. Conti and M. Radici, *Transverse-momentum distributions in a diquark spectator model*, Phys. Rev. D **78** (2008) 074010 [arXiv:0807.0323] [INSPIRE].

[20] A. Bacchetta, M. Radici, F. Conti and M. Guagnelli, *Weighted azimuthal asymmetries in a diquark spectator model*, *Eur. Phys. J. A* **45** (2010) 373 [arXiv:1003.1328] [INSPIRE].

[21] M. Wakamatsu, *Transverse momentum distributions of quarks in the nucleon from the Chiral Quark Soliton Model*, *Phys. Rev. D* **79** (2009) 094028 [arXiv:0903.1886] [INSPIRE].

[22] A.V. Efremov, P. Schweitzer, O.V. Teryaev and P. Zavada, *The relation between TMDs and PDFs in the covariant parton model approach*, *Phys. Rev. D* **83** (2011) 054025 [arXiv:1012.5296] [INSPIRE].

[23] C. Bourrely, F. Buccella and J. Soffer, *Semiinclusive DIS cross sections and spin asymmetries in the quantum statistical parton distributions approach*, *Phys. Rev. D* **83** (2011) 074008 [arXiv:1008.5322] [INSPIRE].

[24] H.H. Matevosyan, W. Bentz, I.C. Cloet and A.W. Thomas, *Transverse Momentum Dependent Fragmentation and Quark Distribution Functions from the NJL-jet Model*, *Phys. Rev. D* **85** (2012) 014021 [arXiv:1111.1740] [INSPIRE].

[25] P. Schweitzer, M. Strikman and C. Weiss, *Intrinsic transverse momentum and parton correlations from dynamical chiral symmetry breaking*, *JHEP* **01** (2013) 163 [arXiv:1210.1267] [INSPIRE].

[26] B. Pasquini, S. Cazzaniga and S. Boffi, *Transverse momentum dependent parton distributions in a light-cone quark model*, *Phys. Rev. D* **78** (2008) 034025 [arXiv:0806.2298] [INSPIRE].

[27] C. Lorce, B. Pasquini and M. Vanderhaeghen, *Unified framework for generalized and transverse-momentum dependent parton distributions within a 3Q light-cone picture of the nucleon*, *JHEP* **05** (2011) 041 [arXiv:1102.4704] [INSPIRE].

[28] H. Avakian, A.V. Efremov, P. Schweitzer and F. Yuan, *The transverse momentum dependent distribution functions in the bag model*, *Phys. Rev. D* **81** (2010) 074035 [arXiv:1001.5467] [INSPIRE].

[29] B.U. Musch, P. Hagler, J.W. Negele and A. Schafer, *Exploring quark transverse momentum distributions with lattice QCD*, *Phys. Rev. D* **83** (2011) 094507 [arXiv:1011.1213] [INSPIRE].

[30] A. Signori, A. Bacchetta, M. Radici and G. Schnell, *Investigations into the flavor dependence of partonic transverse momentum*, *JHEP* **11** (2013) 194 [arXiv:1309.3507] [INSPIRE].

[31] A. Bacchetta, G. Bozzi, M. Radici, M. Ritzmann and A. Signori, *Effect of Flavor-Dependent Partonic Transverse Momentum on the Determination of the W Boson Mass in Hadronic Collisions*, *Phys. Lett. B* **788** (2019) 542 [arXiv:1807.02101] [INSPIRE].

[32] G. Bozzi and A. Signori, *Nonperturbative Uncertainties on the Transverse Momentum Distribution of Electroweak Bosons and on the Determination of the Boson Mass at the LHC*, *Adv. High Energy Phys.* **2019** (2019) 2526897 [arXiv:1901.01162] [INSPIRE].

[33] L. Rottoli, P. Torrielli and A. Vicini, *Determination of the W-boson mass at hadron colliders*, *Eur. Phys. J. C* **83** (2023) 948 [arXiv:2301.04059] [INSPIRE].

[34] R. Abdul Khalek et al., *Science Requirements and Detector Concepts for the Electron-Ion Collider: EIC Yellow Report*, *Nucl. Phys. A* **1026** (2022) 122447 [arXiv:2103.05419] [INSPIRE].

[35] R. Abdul Khalek et al., *Snowmass 2021 White Paper: Electron Ion Collider for High Energy Physics*, in the proceedings of the *Snowmass 2021*, Seattle, WA, U.S.A., 17–26 July 2022, arXiv:2203.13199 [INSPIRE].

JHEP08(2024)232

[36] V.D. Burkert et al., *Precision studies of QCD in the low energy domain of the EIC*, *Prog. Part. Nucl. Phys.* **131** (2023) 104032 [arXiv:2211.15746] [INSPIRE].

[37] R. Abir et al., *The case for an EIC Theory Alliance: Theoretical Challenges of the EIC*, arXiv:2305.14572 [INSPIRE].

[38] A. Bacchetta, M. Diehl, K. Goeke, A. Metz, P.J. Mulders and M. Schlegel, *Semi-inclusive deep inelastic scattering at small transverse momentum*, *JHEP* **02** (2007) 093 [hep-ph/0611265] [INSPIRE].

[39] M. Boglione et al., *Mapping the Kinematical Regimes of Semi-Inclusive Deep Inelastic Scattering*, *JHEP* **10** (2019) 122 [arXiv:1904.12882] [INSPIRE].

[40] P.J. Mulders and R.D. Tangerman, *The Complete tree level result up to order $1/Q$ for polarized deep inelastic leptoproduction*, *Nucl. Phys. B* **461** (1996) 197 [hep-ph/9510301] [INSPIRE].

[41] A. Bacchetta, U. D'Alesio, M. Diehl and C.A. Miller, *Single-spin asymmetries: The Trento conventions*, *Phys. Rev. D* **70** (2004) 117504 [hep-ph/0410050] [INSPIRE].

[42] D. Boer et al., *Gluons and the quark sea at high energies: Distributions, polarization, tomography*, arXiv:1108.1713 [INSPIRE].

[43] A. Bacchetta, D. Boer, M. Diehl and P.J. Mulders, *Matches and mismatches in the descriptions of semi-inclusive processes at low and high transverse momentum*, *JHEP* **08** (2008) 023 [arXiv:0803.0227] [INSPIRE].

[44] A. Bacchetta, G. Bozzi, M.G. Echevarria, C. Pisano, A. Prokudin and M. Radici, *Azimuthal asymmetries in unpolarized SIDIS and Drell-Yan processes: a case study towards TMD factorization at subleading twist*, *Phys. Lett. B* **797** (2019) 134850 [arXiv:1906.07037] [INSPIRE].

[45] M. Abele, D. de Florian and W. Vogelsang, *Approximate NNLO QCD corrections to semi-inclusive DIS*, *Phys. Rev. D* **104** (2021) 094046 [arXiv:2109.00847] [INSPIRE].

[46] A. Vladimirov, *Kinematic power corrections in TMD factorization theorem*, *JHEP* **12** (2023) 008 [arXiv:2307.13054] [INSPIRE].

[47] J. Collins, *Foundations of Perturbative QCD*, in *Cambridge Monographs on Particle Physics, Nuclear Physics and Cosmology* **32**, Cambridge University Press (2023) [DOI:10.1017/9781009401845] [INSPIRE].

[48] M.G. Echevarria, A. Idilbi and I. Scimemi, *Factorization Theorem For Drell-Yan At Low q_T And Transverse Momentum Distributions On-The-Light-Cone*, *JHEP* **07** (2012) 002 [arXiv:1111.4996] [INSPIRE].

[49] M. Grewal, Z.-B. Kang, J.-W. Qiu and A. Signori, *Predictive power of transverse-momentum-dependent distributions*, *Phys. Rev. D* **101** (2020) 114023 [arXiv:2003.07453] [INSPIRE].

[50] T.C. Rogers, *An overview of transverse-momentum-dependent factorization and evolution*, *Eur. Phys. J. A* **52** (2016) 153 [arXiv:1509.04766] [INSPIRE].

[51] I. Scimemi and A. Vladimirov, *Systematic analysis of double-scale evolution*, *JHEP* **08** (2018) 003 [arXiv:1803.11089] [INSPIRE].

[52] W. Bizon, P.F. Monni, E. Re, L. Rottoli and P. Torrielli, *Momentum-space resummation for transverse observables and the Higgs $p_\perp$ at N^3LL+NNLO*, *JHEP* **02** (2018) 108 [arXiv:1705.09127] [INSPIRE].

[53] S. Camarda et al., *DYTurbo: Fast predictions for Drell-Yan processes*, *Eur. Phys. J. C* **80** (2020) 251 [*Erratum ibid.* **80** (2020) 440] [arXiv:1910.07049] [INSPIRE].

[54] G. Bozzi, S. Catani, D. de Florian and M. Grazzini, *The q_T spectrum of the Higgs boson at the LHC in QCD perturbation theory*, *Phys. Lett. B* **564** (2003) 65 [hep-ph/0302104] [INSPIRE].

[55] G. Bozzi, S. Catani, D. de Florian and M. Grazzini, *Transverse-momentum resummation and the spectrum of the Higgs boson at the LHC*, *Nucl. Phys. B* **737** (2006) 73 [hep-ph/0508068] [INSPIRE].

[56] W. Bizoń et al., *Fiducial distributions in Higgs and Drell-Yan production at $N^3LL+NNLO$*, *JHEP* **12** (2018) 132 [arXiv:1805.05916] [INSPIRE].

[57] S. Catani, M.L. Mangano, P. Nason and L. Trentadue, *The Resummation of soft gluons in hadronic collisions*, *Nucl. Phys. B* **478** (1996) 273 [hep-ph/9604351] [INSPIRE].

[58] G. Moreno et al., *Dimuon Production in Proton-Copper Collisions at $\sqrt{s} = 38.8$ GeV*, *Phys. Rev. D* **43** (1991) 2815 [INSPIRE].

[59] E772 collaboration, *Cross-sections for the production of high mass muon pairs from* 800 *GeV proton bombardment of ^2H*, *Phys. Rev. D* **50** (1994) 3038 [*Erratum ibid.* **60** (1999) 119903] [INSPIRE].

[60] A.S. Ito et al., *Measurement of the Continuum of Dimuons Produced in High-Energy Proton-Nucleus Collisions*, *Phys. Rev. D* **23** (1981) 604 [INSPIRE].

[61] STAR collaboration, *Measurements of the Z^0/γ^* cross section and transverse single spin asymmetry in* 510 *GeV $p+p$ collisions*, *Phys. Lett. B* **854** (2024) 138715 [arXiv:2308.15496] [INSPIRE].

[62] PHENIX collaboration, *Measurements of $\mu\mu$ pairs from open heavy flavor and Drell-Yan in $p+p$ collisions at $\sqrt{s} = 200$ GeV*, *Phys. Rev. D* **99** (2019) 072003 [arXiv:1805.02448] [INSPIRE].

[63] CDF collaboration, *The transverse momentum and total cross section of e^+e^- pairs in the Z boson region from $p\bar{p}$ collisions at $\sqrt{s} = 1.8$ TeV*, *Phys. Rev. Lett.* **84** (2000) 845 [hep-ex/0001021] [INSPIRE].

[64] CDF collaboration, *Transverse momentum cross section of e^+e^- pairs in the Z-boson region from $p\bar{p}$ collisions at $\sqrt{s} = 1.96$ TeV*, *Phys. Rev. D* **86** (2012) 052010 [arXiv:1207.7138] [INSPIRE].

[65] D0 collaboration, *Measurement of the inclusive differential cross section for Z bosons as a function of transverse momentum in $\bar{p}p$ collisions at $\sqrt{s} = 1.8$ TeV*, *Phys. Rev. D* **61** (2000) 032004 [hep-ex/9907009] [INSPIRE].

[66] D0 collaboration, *Measurement of the shape of the boson transverse momentum distribution in $p\bar{p} \to Z/\gamma^* \to e^+e^- + X$ events produced at $\sqrt{s}$=1.96-TeV*, *Phys. Rev. Lett.* **100** (2008) 102002 [arXiv:0712.0803] [INSPIRE].

[67] D0 collaboration, *Measurement of the Normalized $Z/\gamma^* \to \mu^+\mu^-$ Transverse Momentum Distribution in $p\bar{p}$ Collisions at $\sqrt{s} = 1.96$ TeV*, *Phys. Lett. B* **693** (2010) 522 [arXiv:1006.0618] [INSPIRE].

[68] LHCb collaboration, *Measurement of the forward Z boson production cross-section in pp collisions at $\sqrt{s} = 7$ TeV*, *JHEP* **08** (2015) 039 [arXiv:1505.07024] [INSPIRE].

[69] LHCb collaboration, *Measurement of forward W and Z boson production in pp collisions at $\sqrt{s} = 8$ TeV*, *JHEP* **01** (2016) 155 [arXiv:1511.08039] [INSPIRE].

[70] LHCb collaboration, *Measurement of the forward Z boson production cross-section in pp collisions at $\sqrt{s} = 13$ TeV*, JHEP **09** (2016) 136 [arXiv:1607.06495] [INSPIRE].

[71] CMS collaboration, *Measurement of the Rapidity and Transverse Momentum Distributions of Z Bosons in pp Collisions at $\sqrt{s} = 7$ TeV*, Phys. Rev. D **85** (2012) 032002 [arXiv:1110.4973] [INSPIRE].

[72] CMS collaboration, *Measurement of the transverse momentum spectra of weak vector bosons produced in proton-proton collisions at $\sqrt{s} = 8$ TeV*, JHEP **02** (2017) 096 [arXiv:1606.05864] [INSPIRE].

[73] CMS collaboration, *Measurements of differential Z boson production cross sections in proton-proton collisions at $\sqrt{s} = 13$ TeV*, JHEP **12** (2019) 061 [arXiv:1909.04133] [INSPIRE].

[74] ATLAS collaboration, *Measurement of the Z/γ^* boson transverse momentum distribution in pp collisions at $\sqrt{s} = 7$ TeV with the ATLAS detector*, JHEP **09** (2014) 145 [arXiv:1406.3660] [INSPIRE].

[75] ATLAS collaboration, *Measurement of the transverse momentum and ϕ^*_η distributions of Drell-Yan lepton pairs in proton-proton collisions at $\sqrt{s} = 8$ TeV with the ATLAS detector*, Eur. Phys. J. C **76** (2016) 291 [arXiv:1512.02192] [INSPIRE].

[76] ATLAS collaboration, *Measurement of the transverse momentum distribution of Drell-Yan lepton pairs in proton-proton collisions at $\sqrt{s} = 13$ TeV with the ATLAS detector*, Eur. Phys. J. C **80** (2020) 616 [arXiv:1912.02844] [INSPIRE].

[77] HERMES collaboration, *Multiplicities of charged pions and kaons from semi-inclusive deep-inelastic scattering by the proton and the deuteron*, Phys. Rev. D **87** (2013) 074029 [arXiv:1212.5407] [INSPIRE].

[78] COMPASS collaboration, *Transverse-momentum-dependent Multiplicities of Charged Hadrons in Muon-Deuteron Deep Inelastic Scattering*, Phys. Rev. D **97** (2018) 032006 [arXiv:1709.07374] [INSPIRE].

[79] A. Buckley et al., *LHAPDF6: parton density access in the LHC precision era*, Eur. Phys. J. C **75** (2015) 132 [arXiv:1412.7420] [INSPIRE].

[80] NNPDF collaboration, *Parton distributions from high-precision collider data*, Eur. Phys. J. C **77** (2017) 663 [arXiv:1706.00428] [INSPIRE].

[81] MAP collaboration, *Pion and kaon fragmentation functions at next-to-next-to-leading order*, Phys. Lett. B **834** (2022) 137456 [arXiv:2204.10331] [INSPIRE].

[82] T. Gutsche, V.E. Lyubovitskij and I. Schmidt, *Nucleon parton distributions in a light-front quark model*, Eur. Phys. J. C **77** (2017) 86 [arXiv:1610.03526] [INSPIRE].

[83] T. Maji and D. Chakrabarti, *Transverse structure of a proton in a light-front quark-diquark model*, Phys. Rev. D **95** (2017) 074009 [arXiv:1702.04557] [INSPIRE].

[84] R. Alessandro, A. Del Dotto, E. Pace, G. Perna, G. Salmè and S. Scopetta, *Light-front transverse momentum distributions for $J = 1/2$ hadronic systems in valence approximation*, Phys. Rev. C **104** (2021) 065204 [arXiv:2107.10187] [INSPIRE].

[85] A.I. Signal and F.G. Cao, *Transverse momentum and transverse momentum distributions in the MIT bag model*, Phys. Lett. B **826** (2022) 136898 [arXiv:2108.12116] [INSPIRE].

[86] A. Bacchetta, L.P. Gamberg, G.R. Goldstein and A. Mukherjee, *Collins fragmentation function for pions and kaons in a spectator model*, Phys. Lett. B **659** (2008) 234 [arXiv:0707.3372] [INSPIRE].

JHEP08(2024)232

[87] L.A. Harland-Lang, A.D. Martin, P. Motylinski and R.S. Thorne, *Parton distributions in the LHC era: MMHT 2014 PDFs*, *Eur. Phys. J. C* **75** (2015) 204 [arXiv:1412.3989] [INSPIRE].

[88] D. de Florian, R. Sassot, M. Epele, R.J. Hernández-Pinto and M. Stratmann, *Parton-to-Pion Fragmentation Reloaded*, *Phys. Rev. D* **91** (2015) 014035 [arXiv:1410.6027] [INSPIRE].

[89] D. de Florian, M. Epele, R.J. Hernandez-Pinto, R. Sassot and M. Stratmann, *Parton-to-Kaon Fragmentation Revisited*, *Phys. Rev. D* **95** (2017) 094019 [arXiv:1702.06353] [INSPIRE].

[90] A. Bacchetta, M.G. Echevarria, P.J.G. Mulders, M. Radici and A. Signori, *Effects of TMD evolution and partonic flavor on e^+e^- annihilation into hadrons*, *JHEP* **11** (2015) 076 [arXiv:1508.00402] [INSPIRE].

[91] M. Boglione, J.O. Gonzalez-Hernandez and R. Taghavi, *Transverse parton momenta in single inclusive hadron production in e^+e^- annihilation processes*, *Phys. Lett. B* **772** (2017) 78 [arXiv:1704.08882] [INSPIRE].

[92] Belle collaboration, *Transverse momentum dependent production cross sections of charged pions, kaons and protons produced in inclusive e^+e^- annihilation at $\sqrt{s} = 10.58$ GeV*, *Phys. Rev. D* **99** (2019) 112006 [arXiv:1902.01552] [INSPIRE].

[93] M. Soleymaninia and H. Khanpour, *Transverse momentum dependent of charged pion, kaon, and proton/antiproton fragmentation functions from e^+e^- annihilation process*, *Phys. Rev. D* **100** (2019) 094033 [arXiv:1907.12294] [INSPIRE].

[94] M. Boglione, J.O. Gonzalez-Hernandez and A. Simonelli, *Transverse momentum dependent fragmentation functions from recent BELLE data*, *Phys. Rev. D* **106** (2022) 074024 [arXiv:2206.08876] [INSPIRE].

[95] J. Collins and T. Rogers, *Understanding the large-distance behavior of transverse-momentum-dependent parton densities and the Collins-Soper evolution kernel*, *Phys. Rev. D* **91** (2015) 074020 [arXiv:1412.3820] [INSPIRE].

[96] F. Hautmann, I. Scimemi and A. Vladimirov, *Non-perturbative contributions to vector-boson transverse momentum spectra in hadronic collisions*, *Phys. Lett. B* **806** (2020) 135478 [arXiv:2002.12810] [INSPIRE].

[97] M. Boglione and A. Simonelli, *Full treatment of the thrust distribution in single inclusive $e^+e^- \to hX$ processes*, *JHEP* **09** (2023) 006 [arXiv:2306.02937] [INSPIRE].

[98] F. Aslan, M. Boglione, J.O. Gonzalez-Hernandez, T. Rainaldi, T.C. Rogers and A. Simonelli, *Phenomenology of TMD parton distributions in Drell-Yan and Z^0 boson production in a hadron structure oriented approach*, arXiv:2401.14266 [INSPIRE].

[99] J. Isaacson, Y. Fu and C.-P. Yuan, *Improving ResBos for the precision needs of the LHC*, arXiv:2311.09916 [INSPIRE].

[100] P. Shanahan, M. Wagman and Y. Zhao, *Collins-Soper kernel for TMD evolution from lattice QCD*, *Phys. Rev. D* **102** (2020) 014511 [arXiv:2003.06063] [INSPIRE].

[101] Lattice Parton collaboration, *Lattice-QCD Calculations of TMD Soft Function Through Large-Momentum Effective Theory*, *Phys. Rev. Lett.* **125** (2020) 192001 [arXiv:2005.14572] [INSPIRE].

[102] M. Schlemmer, A. Vladimirov, C. Zimmermann, M. Engelhardt and A. Schäfer, *Determination of the Collins-Soper Kernel from Lattice QCD*, *JHEP* **08** (2021) 004 [arXiv:2103.16991] [INSPIRE].

JHEP08(2024)232

[103] Y. Li et al., *Lattice QCD Study of Transverse-Momentum Dependent Soft Function*, *Phys. Rev. Lett.* **128** (2022) 062002 [arXiv:2106.13027] [INSPIRE].

[104] P. Shanahan, M. Wagman and Y. Zhao, *Lattice QCD calculation of the Collins-Soper kernel from quasi-TMDPDFs*, *Phys. Rev. D* **104** (2021) 114502 [arXiv:2107.11930] [INSPIRE].

[105] LPC collaboration, *Nonperturbative determination of the Collins-Soper kernel from quasitransverse-momentum-dependent wave functions*, *Phys. Rev. D* **106** (2022) 034509 [arXiv:2204.00200] [INSPIRE].

[106] LPC collaboration, *Renormalization of Transverse-Momentum-Dependent Parton Distribution on the Lattice*, *Phys. Rev. Lett.* **129** (2022) 082002 [arXiv:2205.13402] [INSPIRE].

[107] H.-T. Shu et al., *Universality of the Collins-Soper kernel in lattice calculations*, *Phys. Rev. D* **108** (2023) 074519 [arXiv:2302.06502] [INSPIRE].

[108] LPC collaboration, *Lattice calculation of the intrinsic soft function and the Collins-Soper kernel*, *JHEP* **08** (2023) 172 [arXiv:2306.06488] [INSPIRE].

[109] A. Avkhadiev, P.E. Shanahan, M.L. Wagman and Y. Zhao, *Collins-Soper kernel from lattice QCD at the physical pion mass*, *Phys. Rev. D* **108** (2023) 114505 [arXiv:2307.12359] [INSPIRE].

[110] G. Spanoudes, M. Constantinou and H. Panagopoulos, *Renormalization of asymmetric staple-shaped Wilson-line operators in lattice and continuum perturbation theory*, *Phys. Rev. D* **109** (2024) 114501 [arXiv:2401.01182] [INSPIRE].

[111] A. Avkhadiev, P.E. Shanahan, M.L. Wagman and Y. Zhao, *Determination of the Collins-Soper Kernel from Lattice QCD*, *Phys. Rev. Lett.* **132** (2024) 231901 [arXiv:2402.06725] [INSPIRE].

[112] D. Bollweg, X. Gao, S. Mukherjee and Y. Zhao, *Nonperturbative Collins-Soper kernel from chiral quarks with physical masses*, *Phys. Lett. B* **852** (2024) 138617 [arXiv:2403.00664] [INSPIRE].

[113] D. Boer, L. Gamberg, B. Musch and A. Prokudin, *Bessel-Weighted Asymmetries in Semi Inclusive Deep Inelastic Scattering*, *JHEP* **10** (2011) 021 [arXiv:1107.5294] [INSPIRE].

[114] D. Boer, *Average transverse momentum quantities approaching the lightfront*, *Few-Body Syst.* **56** (2015) 439 [arXiv:1409.8317] [INSPIRE].

[115] CMS collaboration, *Extraction and validation of a new set of CMS PYTHIA8 tunes from underlying-event measurements*, *Eur. Phys. J. C* **80** (2020) 4 [arXiv:1903.12179] [INSPIRE].

[116] I. Bubanja et al., *The small $k_{\rm T}$ region in Drell-Yan production at next-to-leading order with the parton branching method*, *Eur. Phys. J. C* **84** (2024) 154 [arXiv:2312.08655] [INSPIRE].

JHEP08(2024)232